iHALT unlocks liver functionality as a surrogate secondary lymphoid organ

https://doi.org/10.1038/s41586-025-09803-4

Received: 23 January 2025

Accepted: 23 October 2025

Published online: 26 November 2025

Open access

Check for updates

John Gridley[1], David Pak[1], Anuradha Kumari[1], Jacob Shupak[1], Brantley Holland[1], Yifeng Shi[1], Sheetal Trivedi[2], Yongtao Wang[3], Sudhir Pai Kasturi[1], Amit Kapoor[2], Raymond T. Chung[3] & Arash Grakoui[1,4]✉

Upon viral infection, the current paradigm of humoral immunity posits that germinal centre reactions occurring within secondary lymphoid organs (SLOs) yield effector plasma cells that subsequently traffic to infected organs or the bone marrow[1–3]. However, it is not well understood how viral tissue tropism may govern the spatiotemporal dynamics of such responses. Here we demonstrate that infection with a prototypical systemic virus indeed induces liver-trafficking plasma cells generated in SLOs, whereas strictly hepatotropic hepaciviral infection elicits locally primed, virus-specific plasma cells in the liver independently of SLO contribution. Such locally derived progenies emerged from inducible hepatic-associated lymphoid tissue (iHALT) structures containing generative foci of T follicular helper cells, myeloid cells and germinal centre-like B cells, often arising from single founder clones unique to individual periportal structures and locally supporting somatic hypermutation. Critically, the cellular composition, cell–cell contact partners and microarchitecture of such iHALT structures in mice were closely mirrored upon hepaciviral infection in humans. Functionally dependent upon CD40L signalling and cognate B cell receptor specificity, emerging CXCR4^{+}VLA-4^{+}LFA-1^{+}CD44^{+}CD138^{+} plasma cells were immediately retained along CXCL12^{+}fibronectin^{+}ICAM2^{+}osteopontin^{+}type I collagen^{+} periportal fibroblast tracts, acting as cognate anchoring pairs that were critical to their maintenance therein. In summary, we characterize humoral immunity exclusively generated and maintained within its extralymphoid site of viral infection in the liver amidst SLO dormancy, in which functional iHALT successfully compensates for strictly hepatotropic virus-induced SLO-evasion strategies to prevent persistent infection.

Intricately compartmentalized lymphocyte networks exist within SLOs in largely segregated follicular arrangements, benefitting from microarchitectural frameworks that are ideally conducive to their local survival and maintenance. In the context of mounting a T cell-dependent antibody response, the likelihood of experiencing cognate antigen recognition with complementary costimulatory guidance is markedly enhanced in these regions owing to extensive antigen exposure and local trapping mechanisms[4], recirculation of naive lymphocytes with extensive adaptive repertoire diversity, and rational proximity to relevant instructive cell types[5]. Such alignment collectively renders them strategically poised for rapid initiation of de novo humoral responses upon initial antigen encounter in settings of primary infection or immunization. As hubs for B cell affinity maturation, isotype switching and generation of memory B and long-lived plasma cells (LLPCs), the formation of productive germinal centres (GCs) is widely considered to be the unparalleled gold standard for establishment of protective antibody-mediated immunity against most viral infections[6,7]. Given the delicate network of signalling prerequisites that is required for their structural generation and functional orchestration[5], the theme of SLO idealism extends to GCs via provision of growth factors, supportive fibroblastic reticular cell-laden stromal infrastructure[8], conformationally native antigen presentation on follicular dendritic cells[9], and adjacently pre-existing B and T cell zones that are highly malleable to fine-tuned restructuring upon milieu-derived shifts in local chemokine gradients[10]. It therefore seems unlikely and potentially disadvantageous for a host to disregard these rationally pre-formed structures on perpetual retainer in favour of 'starting from scratch' at an extralymphoid site.

Tertiary lymphoid structure (TLS) formation has been observed in settings of chronic inflammation, autoimmunity, cancer and infection. As leukocyte aggregates generated at nonlymphoid sites, TLSs exhibit a wide range of heterogeneity surrounding their precipitating cues, anatomical location, cellular composition and functional outputs. Persistent inflammation is thought to be necessary, but not

---

[1]Division of Microbiology and Immunology, Emory National Primate Research Center, Emory Vaccine Center, Atlanta, GA, USA. [2]Center for Vaccines and Immunity, The Research Institute at Nationwide Children's Hospital, Columbus, OH, USA. [3]Liver Center, Gastrointestinal Division, Massachusetts General Hospital, Harvard Medical School, Boston, MA, USA. [4]Division of Infectious Diseases, Department of Medicine, Emory University School of Medicine, Atlanta, GA, USA. ✉e-mail: arash.grakoui@emory.edu

sufficient, for TLS initiation[11]. As only a subset of patients with cancer develop intratumoural TLSs[12,13], the additional prerequisites for this phenomenon are not well understood. Given that this dichotomy is also present in autoimmunity[14], it is thought that interindividual variability in pro-inflammatory interleukin polymorphisms, inherent stromal propensity for high endothelial venule generation[15], and organ type[16] partially dictate such outcomes. Another key driver of TLS formation and maturation is the presence of antigen, which adopts many forms in these contexts, including self-antigens that have broken central tolerance, tumour-specific markers and foreign pathogens. These factors can culminate in igniting a multistep cascade in which lymphoid tissue inducers activate mesenchymal, fibroblast-like lymphoid tissue organizers to deposit extracellular matrix proteins to form the structural scaffolding of the TLS[17]. Lymphoid tissue inducers also induce proximal vascular endothelium to undergo metaplasia towards high endothelial venule formation, thereby enabling extravasation of circulating lymphocytes to this prepared tissue niche that is conducive to their local congregation. Notably, the anatomical fate of locally derived effector lineages is profoundly altered depending on its origins within SLOs or extralymphoid sites, with each setting cultivating a distinct mixture of sphingosine-1-phosphate (S1P) gradients, chemokines, integrins, extracellular matrix components and adhesion molecules, which collectively dictate local residency, indefinite recirculation or peripheral tissue homing. As tissue–blood immunoglobulin concentration discrepancies have been shown to have marked effects on dichotomous infection outcomes[18], such guided anatomical assignments of plasma cell progenies are likely to be critical determinants of autoimmune severity, tumour repression and resolution of infectious disease.

Locally generated adaptive immunity has been observed in infections of the respiratory tract[19], gut[20], central nervous system[21] and liver[22], among other organs. Most of these cases originate from pre-formed, tissue-adjacent lymphocyte hubs, such as dural-associated lymphoid tissue[23], nasal-associated lymphoid tissue[24] or Peyer's Patches within gut-associated lymphoid tissue[25]. Truly inducible lymphoid structures that are absent in a naive state and form at extralymphoid sites have nonetheless been characterized in the lung, such as inducible bronchus-associated lymphoid tissue during respiratory infection[26] and in the liver during *Ehrlichia muris*[22] or chronic hepatitis C virus (HCV) infection[27]. The majority still of these settings describe a complementary role assumed by locally generated humoral immunity for tandem cooperation with[26] or direct progenitor seeding from[22] SLO-driven responses. Here we utilize a HCV-related rodent hepacivirus (RHV)[28,29], which shares identical genomic structures, polyprotein cleavage patterns and strict hepatotropism with HCV[30,31], to compare the nature of its humoral immune responses to those of systemic viral infection. We thereby characterize humoral immunity generated independently of SLOs that is exclusively confined to its site of acute viral infection amidst SLO dormancy, where iHALT is spontaneously generated in the liver of immunocompetent hosts and is functional in preventing persistent hepaciviral infection.

Humoral immunity confined to the liver

Seeking to determine the anatomical distribution of the functional effectors of antibody-mediated immunity in hepatotropic viral infection, we quantified IgG$^+$ antibody-secreting cells (ASCs) generated during RHV infection. We observed minor fluctuations in peripheral blood mononuclear cells (PBMCs) and spleen throughout infection, but a small and consistently increasing number of ASCs accumulated in the bone marrow, resulting in a 16.1-fold increase by 4 weeks post-infection (Fig. 1a). A relatively delayed expansion of IgG$^+$ ASCs was observed in the liver, with a 1.3-fold increase at day 11 and a 280.6-fold increase by week 4 post-infection (Fig. 1a). Whereas bone marrow ASCs did not show any correlation with splenic ASCs (Fig. 1b), a strong correlation was present when compared with those in the liver (Fig. 1c). This expansion of intrahepatic ASCs coincided with an 8.0-fold increase in serum IgG (Fig. 1d). In further characterizing the anatomical distribution of ASCs during RHV infection, we observed a profoundly skewed tissue preference within the liver at week four post-infection in terms of both total and viral E2-specific IgG ASCs (Fig. 1e,f). To determine whether this liver-focused humoral phenomenon specific to this mouse model, we broadened our analysis to include matched PBMC and liver samples from humans infected with HCV, a close genetic relative of RHV[30,31]. Given the significant skewing in favour of the liver in both RHV infection in mice (Fig. 1h,j) and HCV infections in humans (Fig. 1i,k and Extended Data Fig. 1a–d), this intrahepatic concentration of total and E2-specific IgG ASCs suggests that this represents a conserved response to hepaciviral infection across multiple host species.

SLO dormancy in hepaciviral infection

Although it is well-known that virus-specific plasma cells eventually end up in infected organs, the factors that govern how this process occurs across the spectrum of viral infections with varying organ tropisms are not fully understood. First, to determine whether SLO contributions to the intrahepatic immune response were required components for facilitating hepaciviral clearance, we observed that splenectomized (Fig. 2a,c) and FTY720-treated (Fig. 2b,c) mice were able to acutely resolve RHV infection. These findings demonstrate that both SLO lymphocyte trafficking to the liver and outright splenic presence are dispensable facets of effective anti-RHV immunity. To characterize the origins of RHV- and lymphocytic choriomeningitis (LCMV)-induced intrahepatic ASCs, we initiated FTY720 treatment prior to infection and maintained it throughout to preclude lymphocyte egress from SLOs. Compared with FTY720 treatment, untreated mice exhibited nonsignificant 1.1- and 1.2-fold increases in total IgG (Fig. 2d) and E2-specific (Fig. 2e) ASCs, respectively, in the liver during RHV infection (Fig. 2f). Conversely, untreated mice infected with LCMV generated significant 7.9- and 10.0-fold increases compared with FTY720 treatment in total IgG (Fig. 2g) and viral nucleoprotein-specific (Fig. 2h) ASCs, respectively, in the liver (Fig. 2i). These results support a canonical paradigm of SLO ASC priming with ensuing trafficking to infected organs during systemic infection, whereas strictly hepatotropic infection is conducive to supporting locally generated humoral immunity in the absence of SLO contribution. These observations were not due to the quickly resolving nature of LCMV Armstrong infection, as similar findings were observed with LCMV clone 13 infection (Extended Data Fig. 2a–f). Potential drivers of the lack of such productive iHALT being formed in LCMV infection may include the observed virus localization and lymphocyte restriction near central venules with markedly decreased utilization of oxidative phosphorylation at early time points, in contrast to the periportal preference of RHV and iHALT leukocyte precursors, which exhibit enhanced oxidative phosphorylation usage (Extended Data Figs. 2g–o and 3a,b), representing a classical metabolic signature of GCs[28]. Trafficking of ASCs to the bone marrow following infection with RHV or LCMV was significantly inhibited by FTY720 treatment (Extended Data Fig. 4d–g), suggestive of ASC sequestration in SLOs during LCMV infection and potentially in the liver during RHV infection. This intrahepatic ASC priming in RHV infection prompted us to explore the presence of various cellular components that are typically found in SLO-resident GCs, which revealed significantly enriched populations of GC-like B cells[29] (Fig. 2j and Supplementary Fig. 1a), T follicular helper (T_{FH}) cells (Fig. 2k and Supplementary Fig. 2a) and plasma cells (Fig. 2l and Supplementary Fig. 3a) in the liver during RHV infection. Together, these observations depict two routes by which virus-specific ASCs arrive at infected tissues, that are directly manipulable by spatiotemporal cues of viruses with varying organ tropisms.

After observing locally primed ASC generation in the liver during RHV infection, we sought to characterize the potential role of various signalling prerequisites in initiating this response, including the

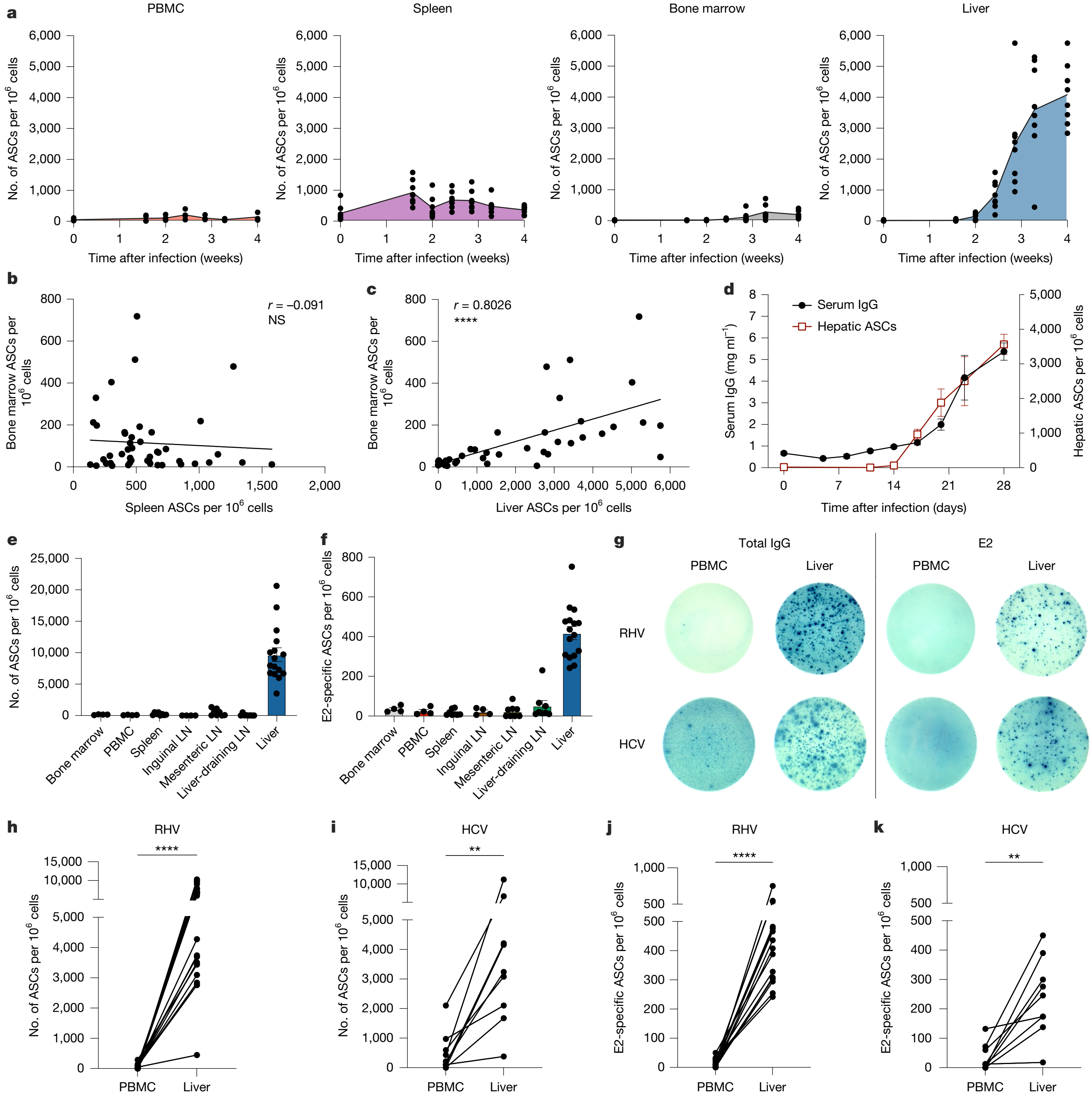

Fig. 1 | Viral-specific humoral responses are primarily compartmentalized within the liver in strictly hepatotropic viral infection. a, Quantification of IgG-secreting ASCs during RHV infection in PBMCs, spleen, bone marrow and liver by ELISpot. Connecting line represents mean values. **b**,**c**, Correlations between bone marrow ASCs and splenic (**b**) or intrahepatic (**c**). Two-tailed nonparametric Spearman correlations with Pearson's *r*. **d**, Serum IgG and intrahepatic ASCs after RHV infection. **e**,**f**, Total (**e**) and E2-specific (**f**) ASCs at 4 weeks post-RHV infection from $n = 2$ independent experiments. LN, lymph node. **g**, Representative ELISpot images of total and E2-specific ASCs in PBMCs and intrahepatic lymphocytes from mice at four weeks post-RHV infection (top) and chronically HCV-infected humans (bottom). **h**–**k**, Quantification of total (**h**,**i**) and E2-specific (**j**,**k**) ASCs from RHV-infected mice (**h**,**j**) and HCV-infected humans (**i**,**k**), with individual-matched paired comparisons shown between PBMCs and intrahepatic lymphocytes. Data from $n = 15$ mice from $n = 2$ independent experiments (**j**) and $n = 9$ individuals (**k**). Two-tailed, paired *t*-test; $P = 0.0082$ (**i**); $P = 0.0019$ (**k**). **a**–**h**,**j**, Mouse data are representative or pooled values from at least two independent experiments with at least three mice per group. **g**,**i**,**k**, Human data include nine individuals chronically infected with HCV. **d**–**f**, Data are mean ± s.e.m. $^{*}P < 0.05$, $^{**}P \leq 0.01$, $^{***}P \leq 0.001$, $^{****}P \leq 0.0001$. NS, not significant ($P < 0.05$).

CD40–CD40L axis, B cell receptor (BCR) specificity and route of initial viral inoculation. We found that CD40L blockade abrogated intrahepatic GC B cell and ASC generation almost entirely (Fig. 2m–o and Extended Data Fig. 4a), thereby implicating CD4^{+} T cell costimulatory instruction as a key upstream mediator of this locally generated humoral response in the liver. Further, such interactions were shown to be critical for facilitating viral clearance, as we observed persistent RHV infection following CD40L blockade (Extended Data Fig. 4b). We then sought to address whether this response was merely a result of bystander, cytokine-induced activation within the infected microenvironment,

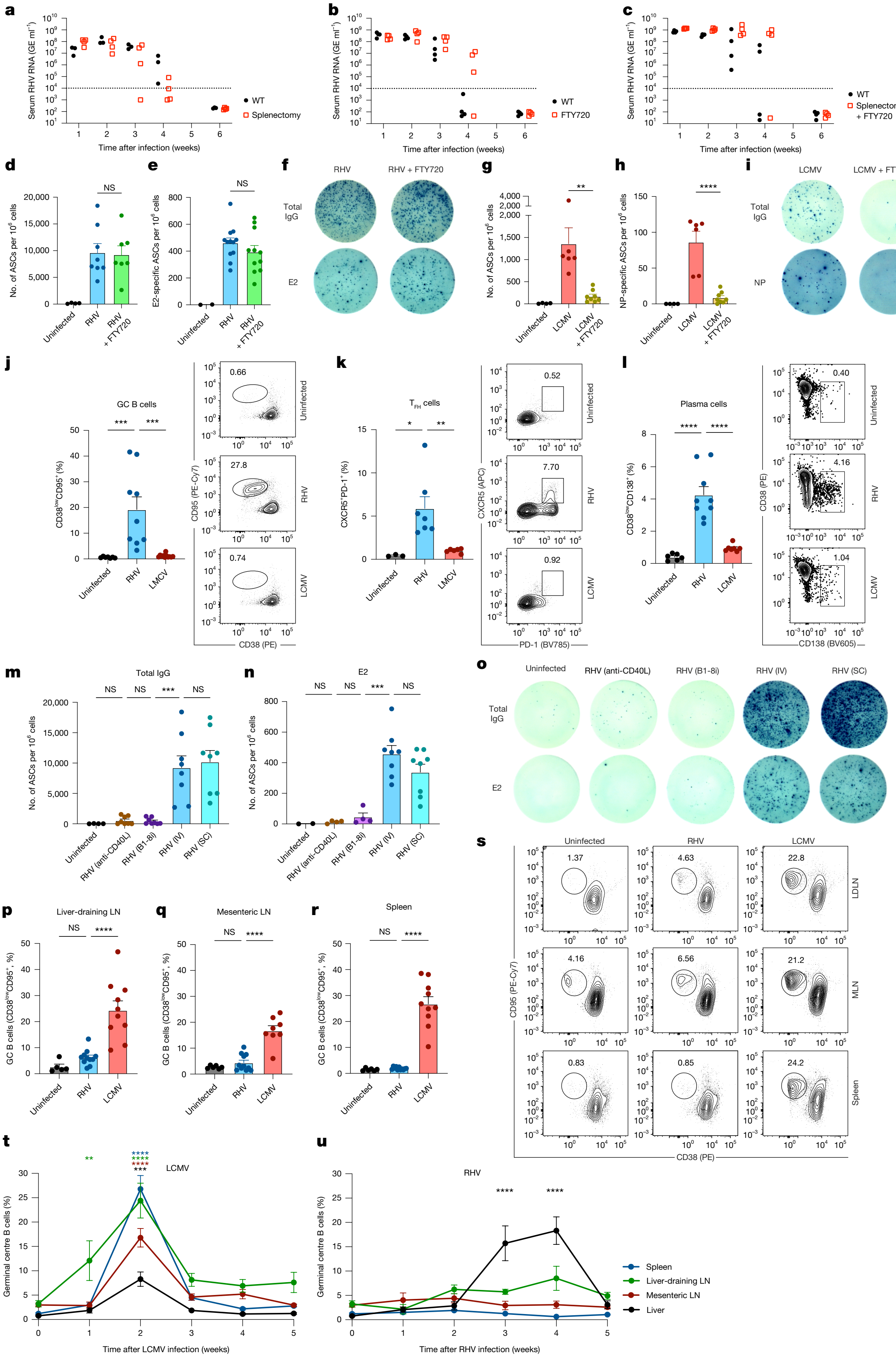

Fig. 2 | See next page for caption.

Fig. 2 | Intrahepatic humoral responses are locally generated amidst SLO dormancy in strictly hepatotropic but not systemic viral infection. **a**–**c**, Serum RHV viraemia in wild-type control (WT) and splenectomized (**a**), FTY720-treated (**b**) or splenectomized FTY720-treated (**c**) mice. GE, genome equivalents. **a**–**i**, FTY720 treatment was initiated one day before infection and continued throughout the experiment. Intrahepatic total (**d**,**g**), RHV E2-specific (**e**) and LCMV Armstrong nucleoprotein (NP)-specific (**h**) ASCs at four weeks post-infection with RHV (**d**,**e**) and LCMV Armstrong (**g**,**h**). **g**, $P = 0.0026$. **f**,**i**, Representative intrahepatic ASC ELISpot images from $n = 2$ independent experiments during RHV (**f**) and LCMV (**i**) infection. NP, viral nucleoprotein. **j**–**l**, Fluorescence-activated cell sorting (FACS) visualization of intrahepatic CD38$^{\text{low}}$CD95^{+} GC B cells (**j**), CXCR5^{+}PD-1^{+} T$_{\text{FH}}$ cells (**k**) and CD38$^{\text{low}}$CD138^{+} plasma cells (**l**) alongside representative plots as a proportion of B cells (**j**,**l**) or CD4^{+} T cells (**k**) from $n = 2$ independent experiments. RHV versus LCMV: $P = 0.0003$ (**j**), $P = 0.0085$ (**k**). **m**–**o**, Intrahepatic total (**m**) and E2-specific (**n**) ASCs at 4 weeks after intravenous (IV) or subcutaneous (SC) RHV infection and representative ELISpot images (**o**) from $n = 2$ independent experiments. RHV B1-8i versus RHV (intravenous): $P = 0.0003$ (**m**), $P = 0.0002$ (**n**). **p**–**r**, CD38$^{\text{low}}$CD95^{+} GC B cell frequencies in liver-draining (**p**) and mesenteric (**q**) lymph nodes and spleen (**r**) at week 2 post-infection alongside representative FACS plots (**s**) from $n = 2$ independent experiments. LDLN, liver-draining lymph node; MLN, mesenteric lymph node. **t**,**u**, Frequency of GC-like B cells after LCMV infection (**t**) and after RHV infection (**u**). Data are mean ± s.e.m. from $n = 2$ independent experiments. **a**–**u**, Data are representative or pooled values from at least two independent experiments with at least three mice per group. Data in **d**,**e**,**g**,**h**, **j**–**n**,**p**–**s** are mean + s.e.m. Two-tailed, unpaired t-test (**d**,**e**,**g**,**h**); one-way ANOVA with Tukey's multiple comparisons test (**j**–**n**,**p**–**r**); two-way ANOVA with Dunnett's multiple comparisons test (**t**,**u**).

thereby enabling bypassing of cognate BCR signalling for B cell activation and ASC differentiation. As B1-8i mice[32], which express a restricted heavy chain specific for 4-hydroxy-3-nitrophenylacetyl, were unable to generate significant levels of ASCs or GC B cells in the liver (Fig. 2m–o and Extended Data Fig. 4a), we therefore demonstrated that antigen-specific BCR signalling was also a critical prerequisite to these liver-generated antibody responses. To delineate whether RHV-induced intrahepatic ASC responses were simply a result of intravenous viral injection owing to inevitably biased delivery and accumulation in the liver, we characterized intrahepatic humoral immunity in mice infected subcutaneously, which we found to largely resemble intravenous infection (Fig. 2m–o and Extended Data Fig. 4a). Such observations suggest that virus-specific, liver-generated ASC formation was uniquely instructed by strictly hepatotropic replication in hepatocytes during RHV infection rather than arising as a by-product of its initial intravenous delivery to the liver.

After determining that the peak of antigen-specific ASC accrual in the liver was rapidly attained by week 2 in LCMV infection, as opposed to the delayed onset and peak at week 4 in RHV infection (Extended Data Fig. 4c), we sought to similarly examine the appearance of GC B cells across various SLOs and the liver over time as a surrogate for potential seeding sites of ASC progenitors prior to hepatic homing or local generation. First, we examined a time point at which GC formation has been robustly observed during prototypical infection and immunization models; at 2 weeks, LCMV infection accordingly elicited significant expansions in GC B cell frequencies compared with naive mice, with 9.0-, 6.2- and 18.1-fold enhancements in the liver-draining lymph node, mesenteric lymph nodes and spleen, respectively (Fig. 2p–s). By contrast, RHV infection induced only modest, nonsignificant increases in each of these SLOs, with 2.3-, 1.6- and 1.3-fold increases in the liver-draining lymph node, mesenteric lymph nodes and spleen, respectively (Fig. 2p–s). Consequently, LCMV infection induced significantly increased GC B cell generation by week 1 in the liver-draining lymph node and in all other organs by week 2 (Fig. 2t), followed by the rapid dissipation of such populations in accordance with the acutely resolving nature of LCMV Armstrong infection. In direct contrast, no significant increase in GC B cell generation was observed throughout the entire duration of RHV infection in the surveyed SLOs, whereas a delayed expansion was observed solely in the liver and immediately extinguished upon viral resolution (Fig. 2u). These findings cooperatively support a route that enables intrahepatic ASCs to arise from SLO-derived GC progenitors during systemic infection, in contrast to locally expanded lineages within the liver during strictly hepatotropic viral infection.

iHALT lacks compartmentalization of SLOs

Upon determining that liver-generated humoral responses require integration of coordinated signalling events and involve classical GC-associated populations amidst SLO dormancy, it was critical to spatially characterize these processes in relation to SLO-driven responses. Accordingly, we performed spatial transcriptomic analyses of the spleen (Fig. 3a) and mesenteric lymph nodes (Fig. 3b) following systemic viral infection, and the liver (Fig. 3c) after strictly hepatotropic viral infection overlaid with haematoxylin and eosin (H&E) staining. Whereas the spleen and lymph nodes exhibited distinctly segmented expression patterns of *Ms4a1* and *CD3g* (Fig. 3d,f), directly coinciding with B cell follicles and T cell zones (Fig. 3i), the liver displayed diffuse overlap and intermingling of such populations without clear borders. Whereas *Siglec1*+ macrophages formed a fine layer inside the marginal zone of the spleen and the subcapsular sinus of lymph nodes as means of antigen sampling for facilitating adaptive immune responses[33], the liver maintained its aberrant cellular distribution patterns with highly disordered myeloid cell scattering (Fig. 3i). Transcripts related to DNA double-stranded breaks[34], DNA repair[35] and cell cycle[36,37] were specifically enriched within GCs in SLOs, including *H2afx*, *Cdk1*, *Mki67*, *Ccna2*, *Nek2*, *Uhrf1* and *Mef2b* (Fig. 3e,i and Extended Data Figs. 5 and 6). As these gene signatures are classically reminiscent of centroblasts undergoing somatic hypermutation (SHM), class-switch recombination and clonal expansion within GCs, these same features were also present within the liver in a subset of GC-like B cells (Fig. 3e,i and Extended Data Fig. 7). Corroborating our previous identification of intrahepatic CD38$^{\text{low}}$CD95$^{\text{hi}}$ B cells bearing a GC-like phenotype[29] (Fig. 2j), this population presented within the liver as central foci of blasting B cells sparsely intertwined with T cells and myeloid lineages, terminally adjacent to differentiated plasma cells as potentially budding progenies (Fig. 3h,i). XBP1^{+} plasma cells were also observed in SLOs as putative outputs of proximally occurring GC reactions, subsequently exiting via bridging channels to the red pulp of the spleen or to the medullary cords in lymph nodes (Fig. 3h,i). Despite lacking multiple structural components of GCs housed within SLOs, iHALT wielded unconventional distribution of unpartitioned, productive foci that were nonetheless competent in robustly manufacturing plasma cell progenies that were immediately tethered to their generative origins.

Anchors locally retain oligoclonal ASCs

Following the local generation of plasma cells within iHALT, it remained unclear what signals were responsible for retaining these cells adjacent to such sites as largely immotile effectors. These populations were relatively absent in the hypoxic zone 3 of the liver surrounding central veins, rather being almost exclusively confined to zone 1 in periportal regions (Extended Data Fig. 8e). Marked expression of putative anchoring pairs at junctions of plasma cells tethered to neighbouring fibroblast tracts included CD44, CXCR4, CD138, αLβ2 integrin (LFA-1) and α4β1 integrin (VLA-4) on plasma cells, complementing osteopontin, CXCL12, type I collagen, ICAM2 and fibronectin, respectively, which were primarily expressed on perivascular fibroblasts (Fig. 4a–d). As several of these cognate binding pairs have previously been demonstrated to mediate LLPC attachment to stromal niches in the bone marrow[1,38–44], this suggested they could be acting similarly here to arrest plasma cell outputs

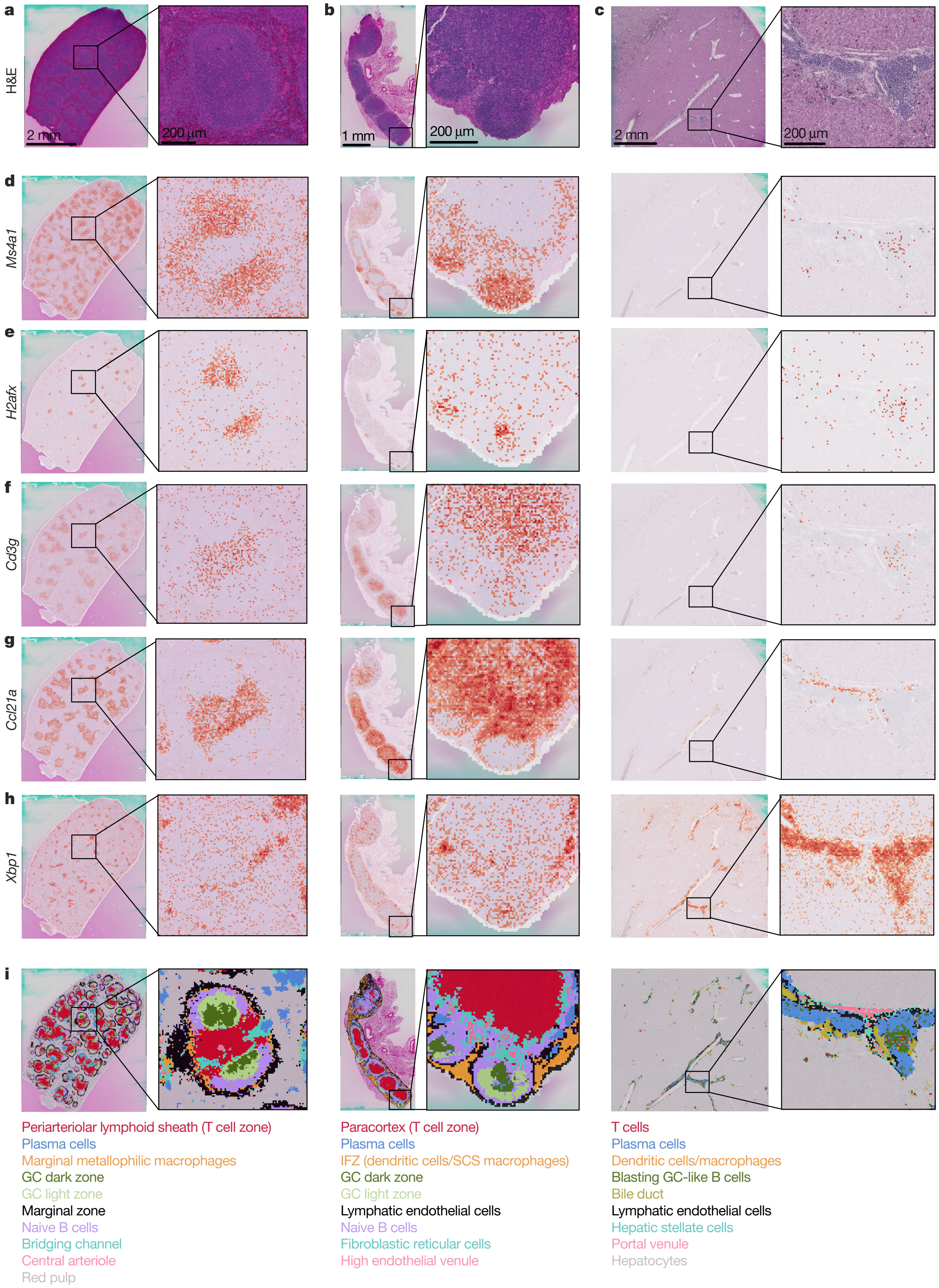

Fig. 3 | iHALT lacks segmented compartmentalization of SLOs but contains functional, generative foci of blasting B cells, giving rise to adjacent plasma cells. a–c, H&E staining of formalin-fixed, paraffin-embedded (FFPE) spleen (**a**) and mesenteric lymph node (**b**) sections at 4 weeks post-LCMV infection and a liver section at 4 weeks post-RHV infection (**c**). Regions of interest (ROIs) are enlarged on the right. One tissue sample from each condition was utilized for Visium HD spatial transcriptomics based on similar morphological H&E staining with limited interindividual variability for $n = 4$ (**a**), $n = 4$ (**b**) and $n = 5$ (**c**) mice. **d–h**, Visium HD spatial transcriptomic of slides shown in **a–c**. Individual transcript localization is shown as $\log_2$-scaled heat maps of 8-µm bins for *Ms4a1* (**d**), *H2afx* (**e**), *Cd3g* (**f**), *Ccl21a* (**g**) and *Xbp1* (**h**). **i**, Graph-based subclustering of clusters of interest from sections in **a–c** were manually annotated and cross-validated with ACT and PanglaoDB cell annotation databases. IFZ, interfollicular zone; SCS, subcapsular sinus. Colours indicate cell type and anatomical zones.

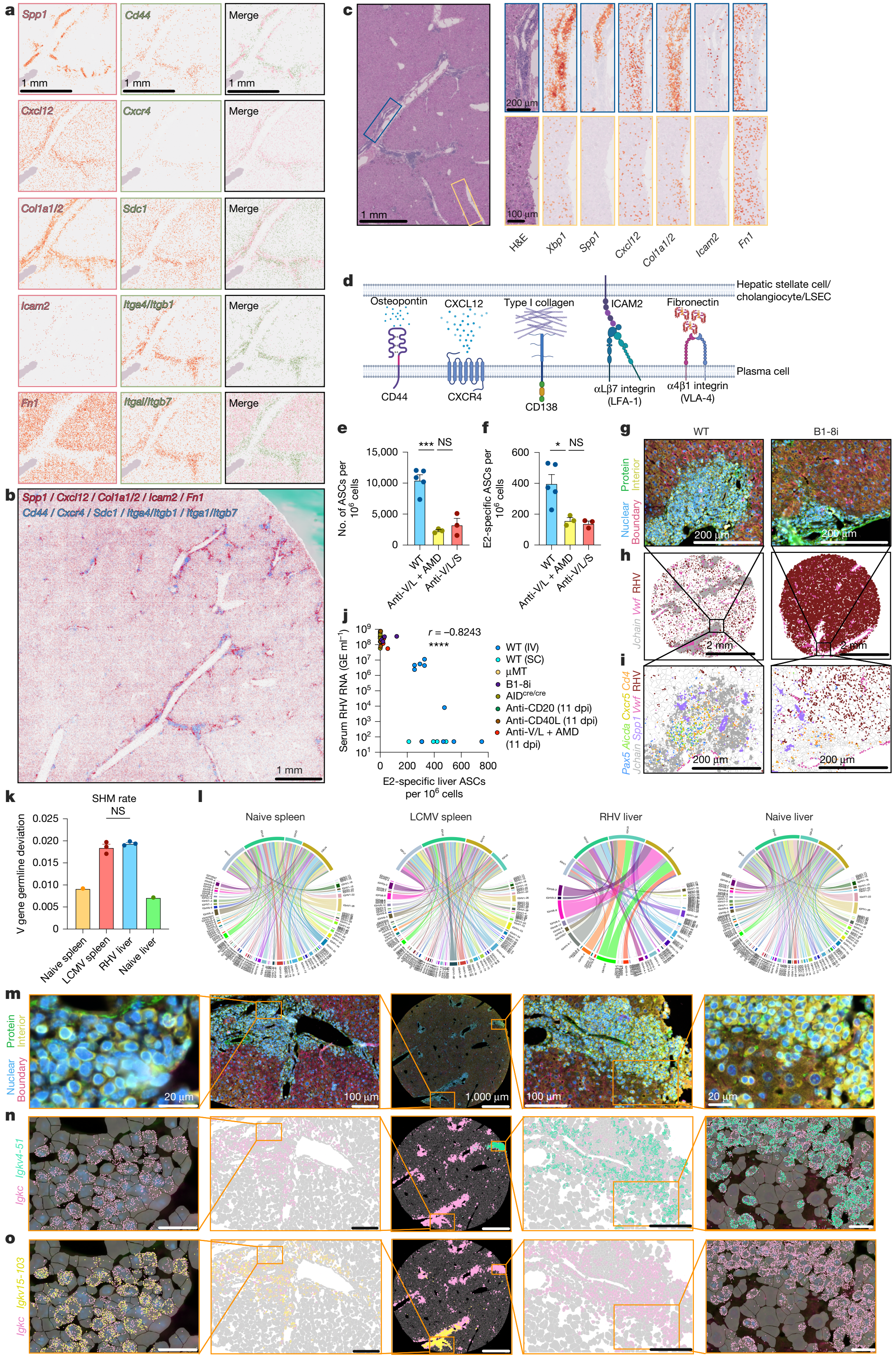

Fig. 4 | See next page for caption.

Fig. 4 | iHALT-derived plasma cells are locally retained and anatomically oligoclonal. a–**c**, Visium HD spatial transcriptomics from liver tissue at four weeks post-RHV infection. **a**, Transcript feature sums of log$_2$-scaled heat maps of 8-µm bins for osteopontin (*Spp1*), *Cxcl12*, type I collagen (*Col1a1* and *Col1a2* (*Col1a1/2*)), *Icam2*, fibronectin (*Fn1*), *Cd44*, *Cxcr4*, CD138 (*Sdc1*), LFA-1 (*Itga4/Itgb1*) and VLA-4 (*Itgal/Itgb7*). **b**, Merged transcript localization of feature sum lists from **a**. **c**, H&E image with portal vein (blue) and central vein (yellow) ROIs (left) with associated transcript localization (right). **d**, Cartoon diagram representing plausible molecular factors responsible for intrahepatic plasma cell retention. LSEC, liver sinusoidal endothelial cell. Created in BioRender. Grakoui, A. (2025) https://BioRender.com/ppmu1j5. **e**,**f**, Intrahepatic total (**e**) and E2-specific (**f**) ASCs at 4 weeks post-infection with or without acute blockade of anchoring molecules at days 26 and 27 post-infection. AMD, AMD3100; anti-V/L, anti-VLA-4 plus anti-LFA-1; anti-V/L/S, anti-VLA-4, anti-LFA-1 plus anti-SPP1. $n = 2$ independent experiments. Control versus anti-V/L + AMD: $P = 0.0003$ (**e**), $P = 0.0182$ (**f**). **g**–**i**, Xenium Prime 5K spatial transcriptomics on liver tissue at three weeks post-infection with upstream morphological staining (**g**), virus, vasculature and plasma cell transcript localization (**h**), and virus, GC-associated and plasma cell transcript localization in periportal regions (**i**). **j**, RHV RNA in serum plotted against intrahepatic E2-specific ASC frequencies at four weeks post-infection. µMT, B6.129S2-Ighmtm1Cgn/J mice lacking mature B cells; dpi, days post infection. **k**,**l**, Bulk IgH BCR sequencing at 4 weeks post-infection from $n = 3$ RHV-infected mice, $n = 3$ LCMV-infected mice and $n = 1$ naive mouse. SHM accrual is plotted as nucleotide divergence from germline sequences among distinct clonotypes (**k**) and IgH V–J gene pairing chord diagrams (**l**). **m**–**o**, Intrahepatic common *Igkc* transcript localization alongside unique Igkv gene family transcripts with upstream morphological staining (**m**) and segmented cell borders showing transcript localization of *Igkc* with *Igkv4-51* (**n**) and *Igkc* with *Igkv15-103* (**o**). **e**,**f**,**j**, Data are representative or pooled values from at least two independent experiments of at least three mice per group. **e**,**f**,**k**, Data are mean + s.e.m. One-way ANOVA with Tukey's multiple comparisons test (**e**,**f**,**k**); two-tailed nonparametric Spearman correlations with Pearson's *r* (**j**).

at their respective origins. Thus, we utilized in vivo disruption of such associative factors, specifically VLA-4, LFA-1 and either CXCR4 or osteopontin, to functionally validate the role of qualitative trends observed from spatial transcriptomics (Fig. 4a–c) in confirming that plasma cell retention in the liver was indeed dependent on such molecular factors (Fig. 4e,f and Supplementary Table 1).

Although virus-specific plasma cells had clearly been shown to be locally generated and retained in this case within the liver, it remained unclear whether these makeshift structures offered functional benefit to the host despite the delayed kinetics and microarchitectural impediments presented by SLO dormancy. Nevertheless, it was readily apparent that generation of functional iHALT was critical for facilitating the resolution of infection amidst a lack of such structures and abundant viral transcripts in B1-8i mice (Fig. 4g–i) and the persistent infection observed following various perturbations precluding intrahepatic ASC generation (Fig. 4j). Such dependence was also corroborated by the unhindered clearance of splenectomized FTY720-treated mice (Fig. 2a–c) and lack of GC formation (Fig. 2p–s,u) or ASCs in SLOs (Fig. 1e,f) in wild-type controls, suggesting that such viral persistence in these cases could be attributable to the overtly clear absence of iHALT (Fig. 4j) in light of the essential role of virus-specific IgG in driving viral resolution[45]. As both the spleen in systemic infection and iHALT in strictly hepatotropic viral infection induced similar levels of SHM over naive controls (Fig. 4k and Extended Data Fig. 9f–i), the spleen retained an evenly expanded, highly polyclonal repertoire, whereas iHALT exhibited marked expansion of a few highly dominant clones (Fig. 4l and Extended Data Fig. 9e). In congruence with such global oligoclonality and the notion of local generation, transcripts of specific BCR variable gene families were predominantly restricted to anatomically unique, isolated iHALT clusters, putatively representative of single founder clones giving rise to ensuing GC-like B cell and plasma cell lineages (Fig. 4m–o and Extended Data Fig. 10h). Collectively, individual iHALT structures were anatomically oligoclonal and supported similar levels of SHM compared with SLOs, ultimately giving rise to plasma cells that were locally retained by functionally validated anchoring molecules and exerted indispensable local antiviral functionality.

Mouse iHALT is closely mirrored in humans

Given our extensive characterization of iHALT induced by mouse hepaciviral infection, it was critical to assess the biological relevance of such findings in humans. Upon performing spatial transcriptomics with subcellular resolution and cell segmentation on liver tissue from healthy, autoimmune hepatitis (AIH), hepatitis B virus (HBV)-infected and HCV-infected humans, we observed leukocytic aggregates that were highly similar within specific conditions yet externally heterogeneous across this spectrum of pathological intrahepatic antigen reservoirs and altogether absent in healthy liver tissue (Fig. 5a,b, Extended Data Fig. 11 and Supplementary Table 2). Although AIH induced large, centralized lymphocytic hubs that were highly interconnected and primarily composed of CD4$^+$ T cells (Fig. 5a–g), its distal margins featured rare waves of CD8$^+$ T cells surrounding and directly engaging intact hepatocytes (Extended Data Fig. 12a,b), potentially representing the effector department of such lymphoid regions in exerting active pathological damage. By contrast, HBV infection featured periportal lymphoid aggregates that were highly internally homogeneous and absent of such obvious segmented compartmentalization phases throughout. Although AIH and HBV induced lymphocytic aggregates that were absent in healthy liver tissue, such regions were highly T cell-dominant (Fig. 5e–g) and presented little evidence of locally generated humoral immunity.

Upon spatially characterizing iHALT during RHV infection with greater resolution and reliable single-cell annotation with related transcript visualization, a plausibly generative hub was observed housing blasting GC-like B cells expressing *Mki67*, *H2afx* and *Aicda* in frequent contact with CD4$^+$ T cells (Fig. 5i,k,m). Notably, HCV-induced lymphoid structures in humans exhibited remarkable similarity to structures observed in mouse RHV infection, featuring a central focus of similarly blasting GC-like B cells in extensive contact with CD4$^+$ T cells (Fig. 5j,l,n). Just outside of these generative foci in both mice and humans, proximally emerging plasma cells were closely retained in the surrounding periportal regions, often directly bordering hepatic stellate cells (Fig. 5o–t). Among such active structures containing GC-like B cells and their ensuing plasma cell counterparts, the highly prominent cell–cell contact patterns favouring GC-like B cells with CD4$^+$ T cells and plasma cells with hepatic stellate cells was again closely recapitulated in mice and humans (Fig. 5h). Collectively, although various settings of liver disease featuring intrahepatic antigen reservoirs elicited lymphoid aggregates of variable composition and organizational structures in humans, hepaciviral infection in mice and humans readily induced lymphoid structures bearing extensive similarity in relation to their cellular composition, cell–cell contact partners and segmented organizational schemes.

Discussion

Virus-specific plasma cells eventually localize within infected organs during the acute phase of a broad spectrum of infections[1,3,46]. As SLOs possess the microarchitectural infrastructure and rationally juxtaposed cells that are necessary for promptly facilitating cooperative GC reactions, infection-induced chemokine gradients and adhesion molecules typically guide such GC-derived effector lineages to these extralymphoid sites of infection. Accordingly, we show here that ASCs are generated in SLOs and subsequently traffic to the infected liver

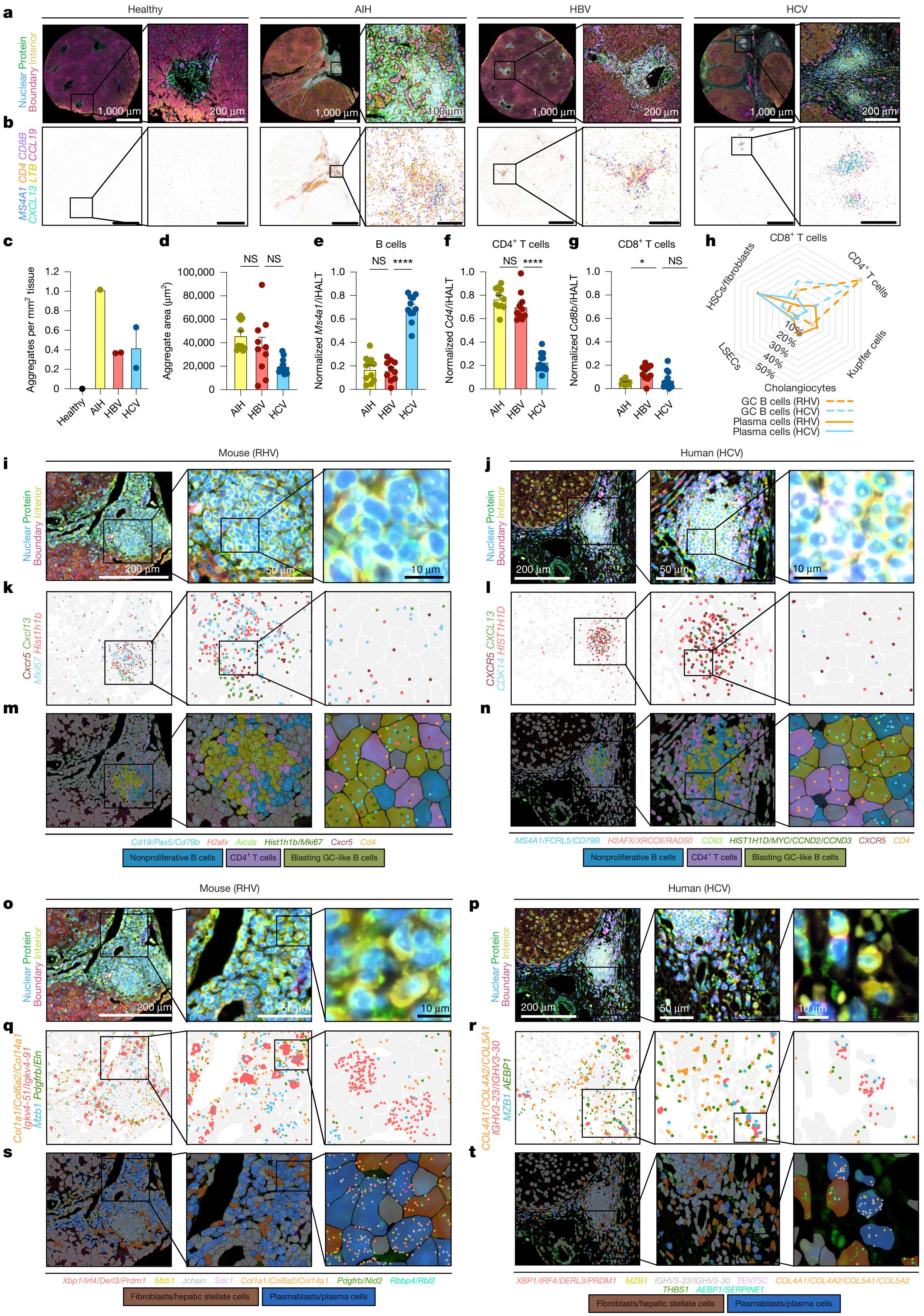

Fig. 5 | See next page for caption.

Fig. 5 | Hepaciviral infection in mouse and human induce intrahepatic lymphoid structures with highly similar cellular composition, organizational microarchitecture and cell–cell contacts. a,**b**, Xenium Prime 5K spatial transcriptomics of liver tissue from healthy, AIH, HBV-infected and HCV-infected humans with upstream staining (**a**) and selected transcript localization (**b**). **c**–**g**, Quantitative analyses from spatial transcriptomics demonstrating number of leukocytic aggregates per mm^2 of tissue (**c**), aggregate area of leukocytic aggregates (**d**), and lymphocytic cell-type proportions of B cells (**e**), CD4$^+$ T cells (**f**) and CD8$^+$ T cells (**g**) observed in leukocytic aggregates from individuals with AIH ($n = 1$), chronic HBV ($n = 2$) and chronic HCV ($n = 2$) infection. Data are mean + s.e.m. **d**–**g**, One-way ANOVA with Tukey's multiple comparisons test. AIH versus HBV: $P = 0.0101$ (**g**). **h**, Quantification of cell types and their direct contact partners within leukocytic aggregates from annotated spatial transcriptomics with subcellular resolution and cell segmentation during mouse RHV (orange) and human HCV (blue) infection. HSC, hepatic stellate cell. **i**–**n**, RHV-infected mouse liver (**i**,**k**,**m**) and HCV-infected human liver (**j**,**l**,**n**) tissue. Generative GC-like structures were characterized upstream staining (**i**,**j**) and GC-associated transcript localization (**k**,**l**) and colour-coded cell-type annotation with selected overlaid transcripts (**m**,**n**). **o**–**t**, RHV-infected mouse liver (**o**,**q**,**s**) and HCV-infected human liver (**p**,**r**,**t**) tissue. Areas of intrahepatic plasma cell residency were characterized by upstream staining (**o**,**p**) and plasma cell and hepatic stellate cell and fibroblast-associated transcripts (**q**,**r**) with colour-coded cell-type annotation (**s**,**t**). Based on similar morphological H&E staining with limited interindividual variability of $n = 2$ HCV-infected humans and $n = 4$ RHV-infected mice, Xenium 5K was performed on tissue from $n = 2$ human and $n = 1$ mouse livers, from which $n = 1$ representative tissue of each are shown in **i**–**t**.

during systemic infection. However, we also characterize humoral immunity that is generated and maintained exclusively at the site of viral infection in the wake of unproductive SLO dormancy and arises spontaneously in immunocompetent hosts as iHALT, which confers protection from persistent hepatotropic viral infection.

As there was minimal humoral activity in SLOs during RHV infection, it was unclear whether this activity was attributable to the strictly hepatotropic nature of this virus. Furthermore, it remained unknown whether this effect was specific to this mouse model or, rather, represented a conserved phenomenon occurring across multiple host species. We therefore utilized human samples from individuals infected with HCV, a close genetic relative of RHV with identical genomic structure and polyprotein cleavage patterns[30], to confirm that an anatomical skewing of E2-specific ASCs in the liver represented a conserved immunological response to hepaciviral infection in both mice and humans. As we have previously shown that CD20$^+$ B cells are critical for RHV clearance prior to two weeks post-infection but dispensable thereafter[45], this suggests that the local differentiation of GC-like B cells to depletion-resistant intrahepatic ASCs at this time is likely to orchestrate IgG-dependent viral resolution. Although these results confirmed the intrahepatic confinement of functional, virus-specific effectors in mice and humans, it was critical to determine to what extent iHALT may be present in this setting as a potentially generative hub of such outputs. Of note, lymphoid structures were readily observed in HCV-infected human liver tissue, demonstrating high similarity to those seen in mouse RHV infection in terms of cellular composition, generalized microarchitectural arrangement and cell–cell contact partners. Given the delayed development of intrahepatic TLS formation and potent neutralizing antibodies in the chronic phase of HCV infection[47,48], it is possible that the timely generation of functional iHALT may dictate perpetual infection outcome prior to the onset of T cell exhaustion[49] and extensive quasispecies diversification[50]. Utilization of RHV to systematically investigate the development of iHALT in an unrestricted fashion and corroborate the biological significance of such findings with static observations in human samples is a highly physiologically relevant mouse model of natural hepatotropic infection and shares multiple features with its hepacivirus relative HCV, including the propensity to cause fibrosis and hepatocellular carcinoma, replicative dependence on host miR-122, identical genomic structures and polyprotein cleavage patterns, strict hepatotropism, viral buoyancy, entry dependence on hepatocyte scavenger receptors and tight junction proteins, correlates of protective adaptive immunity, and the intricacies of iHALT described here and elsewhere[30,31,45,51–54].

Systemic infection ensures extensive antigen exposure in tissues and SLOs via circulating blood, draining lymph and cell–cell contacts[55]. Host immune systems in this setting can therefore generate adaptive immune responses from any of these convenient, rapid and efficient sites. Accordingly, we found that LCMV infection elicited high frequencies of GC B cells in SLOs by one to two weeks post-infection and that intrahepatic ASC accrual was dependent on lymphocyte egress from SLOs. As strictly hepatotropic viral infection conversely did not produce significant ASC or GC B cell responses in SLOs, a delayed generation of GC B cells and T_{FH} cells in the liver at four weeks post-infection supported the development of intrahepatic, virus-specific ASCs that were independent of SLO contribution. Consistent with this apparent lack of functional role, viral clearance was unhindered following combined splenectomy and treatment-induced inhibition of lymphocyte egress from SLOs. As hepatotropic viral infection has been shown to induce a highly inflammatory environment in the liver, it was critical to distinguish whether the humoral responses characterized here were merely by-products of such cytokine-induced bystander activation[56] or, rather, represented coordinated immune interactions crafted by cognate specificity. We proceeded to show that productive iHALT was indeed facilitated by costimulatory guidance, required a diverse, unrestricted BCR repertoire, supported comparable levels of SHM as SLOs, and demonstrated markedly unique oligoclonality among individual periportal structures. Consistent with such signalling intricacies required for functional iHALT orchestration, systemic viral infection of prolonged duration was also unable to elicit locally primed humoral immunity, further reinforcing the notion that kinetically persisting, general inflammation was not alone sufficient to induce iHALT. Extending further to cases of strictly hepatotropic antigen reservoirs, intrahepatic lymphocyte aggregates could be readily visualized during HBV infection and AIH in humans. Although the cellular composition and microarchitecture of these structures deviated markedly from those seen in HCV infection, extensively secreted hepatitis B surface antigen and ensuing effects on systemic antigen availability may contribute to the B cell underrepresentation. Further, although AIH elicited large, centralized CD4$^+$ T cell networks with CD8$^+$ T cells at its peripheral edges surrounding intact hepatocytes, the precise signalling pathways accounting for such heterogeneity across the spectrum of pathological intrahepatic antigen reservoirs and associated disease states remain undefined and represent an intriguing avenue for future study. Given that the local facilitation of hallmark SLO-associated activities such as somatic hypermutation, antigen-specific clonal expansion and plasma cell differentiation were experimentally validated to occur within iHALT alongside downstream functional efficacy of such progenies in exerting antiviral control, such criteria justify its classification as a bona fide inducible lymphoid tissue within the overarching context of TLSs. Such an assignment distinguishes itself from cases restricted to broader, less descript TLS dubbing that are based solely on the observation of leukocytic aggregates of unknown composition, activity, or functionality, thus extending the potential acquisition of iHALT labelling to other pathological settings of experimentally validated SLO mimicry accompanied by functional adaptive effector outputs within the liver.

Regardless of the initial location of adaptive immune effector priming, if and to where the effector cells depart is largely determined by gradients of S1P[57] and various chemokines in conjunction with lymphocyte integrin interaction with local adhesion factors[58]. Essentially, such migratory outcomes are dictated by the competitive proceedings of multiple individual factors vying for control to their own end, such as the increased LFA-1 and VLA-4 integrin expression collectively overpowering potential S1PR1 responsiveness in ultimately maintaining marginal zone B cells as a non-recirculating population in the spleen[59,60]. As GC-derived plasma cells in the spleen exiting through the bridging channels can traffic to infected organs via CXCR3[46] or permanently arrest at CXCL12-rich regions internally in the red pulp[38] or externally in the bone marrow[38], the specific set of guiding principles present in the liver for locally produced iHALT progenies warranted further investigation. Although iHALT formally lacks multiple cellular components and the segregated compartmentalization of bona fide SLO GCs, it possesses a central, integrative network of GC dark zone-like, blasting B cells, T cells and myeloid cells immediately surrounded by budding plasma cell outputs. In contrast to transitory bridging channels of the spleen or distant medullary sinuses of lymph nodes, the majority of plasma cells in the liver were directly confined to their generative origins within the parenchyma along neighbouring periportal tracts. Consistent with this local maintenance and the aforementioned multivariable function dictating the anatomical fate of plasma cells, these intrahepatic regions shared many of the same features responsible for LLPC tethering to bone marrow stromal niches. Namely, iHALT-derived plasma cells expressed high levels of CD44, CXCR4, CD138, LFA-1 and VLA-4, and directly juxtaposed perivascular fibroblast tracts were high producers of their respective ligand pairs, including osteopontin[42], CXCL12[38], type I collagen[39], ICAM2[43] and fibronectin[44]. Furthermore, plasma cell accrual was rarely observed near central veins in zone 3 of the liver, suggesting that the more highly oxygenated zone 1 periportal regions are inherently more conducive to fostering iHALT development. In light of the concentrated anatomical skewing of functional, virus-specific ASCs in the liver demonstrated to be both locally produced and retained, such molecular anchoring pairs were functionally validated in vivo as significant contributors to plasma cell retention in the liver in direct adjacency to their generative foci in lieu of succumbing to S1PR1-dependent egress to circulation.

Despite forfeiting the rapid kinetics and stromal intricacy of SLO-generated antibody responses, local TLS formation at sites of infection or within tumours claims its own set of unique, potentially compensatory advantages. Locally relevant antigen biasing can facilitate a higher likelihood of cognate lymphocyte recognition focused exclusively on targets of interest in a confined, antigenically concentrated region and, further, ensuing effector lineages are immediately spatially poised for local, potent antibody production without migratory hurdles or suboptimal concentration discrepancies between blood and tissue[18]. As viruses adopt multiple strategies to prolong infection duration and thereby increase the likelihood of quasispecies diversification and T cell exhaustion in order to achieve chronicity, it is plausible that some viruses may exploit perceived host vulnerabilities to delay adaptive immune responses via SLO subversion in settings of strict replicative organ tropism. Here we characterize locally retained humoral immunity that is generated exclusively at its extralymphoid site of infection and is able to compensate for virus-mediated, covert suppression of SLO activity to derail persistent infection.

Online content

Any methods, additional references, Nature Portfolio reporting summaries, source data, extended data, supplementary information, acknowledgements, peer review information; details of author contributions and competing interests; and statements of data and code availability are available at https://doi.org/10.1038/s41586-025-09803-4.

1. Kunkel, E. J. & Butcher, E. C. Plasma-cell homing. *Nat. Rev. Immunol.* **3**, 822–829 (2003).
2. Tarlinton, D. M., Ding, Z., Tellier, J. & Nutt, S. L. Making sense of plasma cell heterogeneity. *Curr. Opin. Immunol.* **81**, 102297 (2023).
3. Wellford, S. A. et al. Mucosal plasma cells are required to protect the upper airway and brain from infection. *Immunity* **55**, 2118–2134.e6 (2022).
4. Pereira, J. P., Kelly, L. M. & Cyster, J. G. Finding the right niche: B-cell migration in the early phases of T-dependent antibody responses. *Int. Immunol.* **22**, 413–419 (2010).
5. Victora, G. D. & Nussenzweig, M. C. Germinal Centers. *Annu. Rev. Immunol.* **40**, 413–442 (2022).
6. Kim, G. et al. Germinal center-induced immunity is correlated with protection against SARS-CoV-2 reinfection but not lung damage. *J. Infect. Dis.* **224**, 1861–1872 (2021).
7. Swain, S. L., McKinstry, K. K. & Strutt, T. M. Expanding roles for CD4$^+$ T cells in immunity to viruses. *Nat. Rev. Immunol.* **12**, 136–148 (2012).
8. Acton, S. E., Onder, L., Novkovic, M., Martinez, V. G. & Ludewig, B. Communication, construction, and fluid control: lymphoid organ fibroblastic reticular cell and conduit networks. *Trends Immunol.* **42**, 782–794 (2021).
9. Heesters, B. A., van der Poel, C. E., Das, A. & Carroll, M. C. Antigen presentation to B cells. *Trends Immunol.* **37**, 844–854 (2016).
10. Cyster, J. G. Chemokines and cell migration in secondary lymphoid organs. *Science* **286**, 2098–2102 (1999).
11. Khanal, S., Wieland, A. & Gunderson, A. J. Mechanisms of tertiary lymphoid structure formation: cooperation between inflammation and antigenicity. *Front. Immunol.* **14**, 1267654 (2023).
12. Sautès-Fridman, C., Petitprez, F., Calderaro, J. & Fridman, W. H. Tertiary lymphoid structures in the era of cancer immunotherapy. *Nat. Rev. Cancer* **19**, 307–325 (2019).
13. Shu, D. H. et al. Immunotherapy response induces divergent tertiary lymphoid structure morphologies in hepatocellular carcinoma. *Nat. Immunol.* **25**, 2110–2123 (2024).
14. Neyt, K., Perros, F., GeurtsvanKessel, C. H., Hammad, H. & Lambrecht, B. N. Tertiary lymphoid organs in infection and autoimmunity. *Trends Immunol.* **33**, 297–305 (2012).
15. Stranford, S. & Ruddle, N. H. Follicular dendritic cells, conduits, lymphatic vessels, and high endothelial venules in tertiary lymphoid organs: parallels with lymph node stroma. *Front. Immunol.* **3**, 350 (2012).
16. Rodriguez, A. B. et al. Immune mechanisms orchestrate tertiary lymphoid structures in tumors via cancer-associated fibroblasts. *Cell Rep.* **36**, 109422 (2021).
17. Zhao, L. et al. Tertiary lymphoid structures in diseases: immune mechanisms and therapeutic advances. *Signal Transduct. Target. Ther.* **9**, 225 (2024).
18. Tai, W. et al. A lung-selective delivery of mRNA encoding broadly neutralizing antibody against SARS-CoV-2 infection. *Nat. Commun.* **14**, 8042 (2023).
19. Silva-Sanchez, A. & Randall, T. D. Role of iBALT in respiratory immunity. *Curr. Top. Microbiol. Immunol.* **426**, 21–43 (2020).
20. Bemark, M., Pitcher, M. J., Dionisi, C. & Spencer, J. Gut-associated lymphoid tissue: a microbiota-driven hub of B cell immunity. *Trends Immunol.* **45**, 211–223 (2024).
21. Fitzpatrick, Z. et al. Venous-plexus-associated lymphoid hubs support meningeal humoral immunity. *Nature* **628**, 612–619 (2024).
22. Trivedi, N. et al. Liver is a generative site for the B cell response to *Ehrlichia muris*. *Immunity* **51**, 1088–1101.e1085 (2019).
23. Park, J. H., Alexander, J. F., Smyth, L. C. D. & Kipnis, J. DALT: the brain's border patrol. *Cell Res.* **34**, 603–604 (2024).
24. Spit, B. J., Hendriksen, E. G., Bruijntjes, J. P. & Kuper, C. F. Nasal lymphoid tissue in the rat. *Cell Tissue Res.* **255**, 193–198 (1989).
25. Jung, C., Hugot, J. P. & Barreau, F. Peyer's patches: the immune sensors of the intestine. *Int. J. Inflam.* **2010**, 823710 (2010).
26. Moyron-Quiroz, J. E. et al. Role of inducible bronchus associated lymphoid tissue (iBALT) in respiratory immunity. *Nat. Med.* **10**, 927–934 (2004).
27. Mosnier, J. F. et al. The intraportal lymphoid nodule and its environment in chronic active hepatitis C: an immunohistochemical study. *Hepatology* **17**, 366–371 (1993).
28. Choi, S. C. & Morel, L. Immune metabolism regulation of the germinal center response. *Exp. Mol. Med.* **52**, 348–355 (2020).
29. Tas, J. M. J. et al. Antibodies from primary humoral responses modulate the recruitment of naive B cells during secondary responses. *Immunity* **55**, 1856–1871.e6 (2022).
30. Trivedi, S. et al. Viral persistence, liver disease, and host response in a hepatitis C-like virus rat model. *Hepatology* **68**, 435–448 (2018).
31. Billerbeck, E. et al. Mouse models of acute and chronic hepacivirus infection. *Science* **357**, 204–208 (2017).
32. Sonoda, E. et al. B cell development under the condition of allelic inclusion. *Immunity* **6**, 225–233 (1997).
33. Moran, I., Grootveld, A. K., Nguyen, A. & Phan, T. G. Subcapsular sinus macrophages: the seat of innate and adaptive memory in murine lymph nodes. *Trends Immunol.* **40**, 35–48 (2019).
34. Collins, P. L. et al. DNA double-strand breaks induce H2Ax phosphorylation domains in a contact-dependent manner. *Nat. Commun.* **11**, 3158 (2020).
35. Kciuk, M., Gielecińska, A., Mujwar, S., Mojzych, M. & Kontek, R. Cyclin-dependent kinases in DNA damage response. *Biochim. Biophys. Acta, Rev. Cancer* **1877**, 188716 (2022).
36. Chen, C. et al. Uhrf1 regulates germinal center B cell expansion and affinity maturation to control viral infection. *J. Exp. Med.* **215**, 1437–1448 (2018).
37. Maguire, A. et al. Enhanced DNA repair and genomic stability identify a novel HIV-related diffuse large B-cell lymphoma signature. *Int. J. Cancer* **145**, 3078–3088 (2019).
38. Hargreaves, D. C. et al. A coordinated change in chemokine responsiveness guides plasma cell movements. *J. Exp. Med.* **194**, 45–56 (2001).
39. Ridley, R. C. et al. Expression of syndecan regulates human myeloma plasma cell adhesion to type I collagen. *Blood* **81**, 767–774 (1993).
40. Zehentmeier, S. et al. Static and dynamic components synergize to form a stable survival niche for bone marrow plasma cells. *Eur. J. Immunol.* **44**, 2306–2317 (2014).
41. Khodadadi, L., Cheng, Q., Radbruch, A. & Hiepe, F. The maintenance of memory plasma cells. *Front. Immunol.* **10**, 721 (2019).
42. Hui, T., Sørensen, E. S. & Rittling, S. R. Osteopontin binding to the alpha 4 integrin requires highest affinity integrin conformation, but is independent of post-translational modifications of osteopontin. *Matrix Biol.* **41**, 19–25 (2015).
43. Staunton, D. E., Dustin, M. L. & Springer, T. A. Functional cloning of ICAM-2, a cell adhesion ligand for LFA-1 homologous to ICAM-1. *Nature* **339**, 61–64 (1989).

44. Matsunaga, T. et al. Interaction between leukemic-cell VLA-4 and stromal fibronectin is a decisive factor for minimal residual disease of acute myelogenous leukemia. *Nat. Med.* **9**, 1158–1165 (2003).
45. Gridley, J. et al. Concerted synergy between viral-specific IgG and CD8 + T cells is critical for clearance of an HCV-related rodent hepacivirus. *Hepatology* **80**, 937–950 (2024).
46. Marques, C. P. et al. CXCR3-dependent plasma blast migration to the central nervous system during viral encephalomyelitis. *J. Virol.* **85**, 6136–6147 (2011).
47. Freni, M. A. et al. Focal lymphocytic aggregates in chronic hepatitis C: occurrence, immunohistochemical characterization, and relation to markers of autoimmunity. *Hepatology* **22**, 389–394 (1995).
48. Logvinoff, C. et al. Neutralizing antibody response during acute and chronic hepatitis C virus infection. *Proc. Natl Acad. Sci. USA* **101**, 10149–10154 (2004).
49. Raghuraman, S. et al. Spontaneous clearance of chronic hepatitis C virus infection is associated with appearance of neutralizing antibodies and reversal of T-cell exhaustion. *J. Infect. Dis.* **205**, 763–771 (2012).
50. Koizumi, K. et al. Diversity of quasispecies in various disease stages of chronic hepatitis C virus infection and its significance in interferon treatment. *Hepatology* **22**, 30–35 (1995).
51. Dravid, P. et al. Phenotype and fate of liver-resident CD8 T cells during acute and chronic hepacivirus infection. *PLoS Pathog.* **19**, e1011697 (2023).
52. Wolfisberg, R. et al. Replicons of a rodent hepatitis C model virus permit selection of highly permissive cells. *J. Virol.* https://doi.org/10.1128/jvi.00733-19 (2019).
53. Wolfisberg, R. et al. Neutralization and receptor use of infectious culture-derived rat hepacivirus as a model for HCV. *Hepatology* **76**, 1506–1519 (2022).
54. Tanaka, T. et al. Identification of claudin-3 as an entry factor for rat hepacivirus. *Proc. Natl Acad. Sci. USA* **122**, e2508736122 (2025).
55. Akkaya, M., Kwak, K. & Pierce, S. K. B cell memory: building two walls of protection against pathogens. *Nat. Rev. Immunol.* **20**, 229–238 (2020).
56. Jiang, W. et al. COVID-19 is associated with bystander polyclonal autoreactive B cell activation as reflected by a broad autoantibody production, but none is linked to disease severity. *J. Med. Virol.* **95**, e28134 (2023).
57. Mandala, S. et al. Alteration of lymphocyte trafficking by sphingosine-1-phosphate receptor agonists. *Science* **296**, 346–349 (2002).
58. Fooksman, D. R. et al. Development and migration of plasma cells in the mouse lymph node. *Immunity* **33**, 118–127 (2010).
59. Lu, T. T. & Cyster, J. G. Integrin-mediated long-term B cell retention in the splenic marginal zone. *Science* **297**, 409–412 (2002).
60. Arnon, T. I., Horton, R. M., Grigorova, I. L. & Cyster, J. G. Visualization of splenic marginal zone B-cell shuttling and follicular B-cell egress. *Nature* **493**, 684–688 (2013).

Publisher's note Springer Nature remains neutral with regard to jurisdictional claims in published maps and institutional affiliations.

Open Access This article is licensed under a Creative Commons Attribution-NonCommercial-NoDerivatives 4.0 International License, which permits any non-commercial use, sharing, distribution and reproduction in any medium or format, as long as you give appropriate credit to the original author(s) and the source, provide a link to the Creative Commons licence, and indicate if you modified the licensed material. You do not have permission under this licence to share adapted material derived from this article or parts of it. The images or other third party material in this article are included in the article's Creative Commons licence, unless indicated otherwise in a credit line to the material. If material is not included in the article's Creative Commons licence and your intended use is not permitted by statutory regulation or exceeds the permitted use, you will need to obtain permission directly from the copyright holder. To view a copy of this licence, visit http://creativecommons.org/licenses/by-nc-nd/4.0/.

© The Author(s) 2025

Methods

Human study participants

Patients undergoing orthotopic liver transplantation at Emory Transplant Center of Emory University Hospital were enrolled in the study in accordance with the Emory University Institutional Review Board (IRB) approval (IRB #00100485). HCV-infected samples utilized in the current study are from individuals chronically infected with HCV without HIV coinfection. Patient characteristics with clinical information and relevant biological variables are summarized in Supplementary Table 1. Written informed consent was obtained from each individual and IRB #00100485 conforms to the guidelines of the 1975 Declaration of Helsinki (revised 2013). Additional human liver samples were obtained in accordance with the protocol approved by the Mass General Brigham IRB, protocol nos. 1999P004983 and 2004P000793.

Animals and ethics statement

C57BL/6J and B6.129P2-*Aicda*$^{tm1(cre)Mnz}$/J (AID$^{cre/cre}$) mice were obtained from Jackson Laboratories. B6.129P2[C]-Ightm2Cgn/J (B1-8i) mice were obtained from J. Jacob. Predetermined sample size calculations and blinding were not performed, as number of individual data points and experimental design were determined based on experiment type to generate interpretable, reproducible conclusions. Regarding randomization, age-matched mice of identical strains ordered from commercial vendors were randomly divided into cages by animal care staff upon arrival at vivarium facilities. Mice were six to ten weeks of age at the time of study initiation. All biohazard and animal experiments were carried out in accordance with approved protocols from the Emory Institutional Animal Care and Use Committee (IACUC #201700372).

Viruses and infections

RHV inoculum was generated in vivo following serial passage and adaptation to the mouse host. Mice were infected with RHV via retroorbital injection unless otherwise specified with 10^5 viral genome equivalents. Lymphocytic choriomeningitis virus (LCMV) Armstrong was infected intraperitoneally with 2×10^5 plaque-forming units (PFU) per mouse and LCMV clone 13 was infected via retroorbital injection with 2×10^6 PFU per mouse.

FTY720 treatment and CD40L blockade

To prevent lymphocyte egress from SLOs, FTY720 (Sigma) was administered at a final concentration of 1 mg kg^{-1} and injected intraperitoneally three times weekly. To disrupt CD40–CD40L signalling, 250 µg anti-CD154 (CD40L, clone MR1, InVivoMab) was injected intraperitoneally 3 times weekly.

Disruption of associative anchor molecules

For assessing the functional role of cognate associa designated slide area. These slides were processed tive anchoring pairs on intrahepatic plasma cell retention, interventional treatments were acutely administered intraperitoneally at 200 µg each on days 26 and day 27 post-infection, after which ASC enumeration was conducted at day 28 post-infection. Such interventions included specified combinations of anti-CD49d (VLA-4, clone PS/2, InVivoMab), anti-CD11a (LFA-1, clone M17/4, InVivoMab), anti-SPP1 (osteopontin, clone 103D6, InVivoMab), and AMD3100 octahydrochloride (Tocris Bioscience). Persistent disruption of such factors was achieved via administration of such treatment at 100 µg 3 times weekly beginning at day 11 post-infection, again being assessed for intrahepatic ASC generation at day 28 post-infection.

Splenectomy

To eliminate splenic antiviral contributions, mice were subjected to general anaesthesia with nebulized isoflurane, after which the spleen was exteriorized and separated from proximal mesentery and vasculature by cauterization. Mice were given postoperative analgesia and permitted to recover for one week prior to infection.

Virus quantification

RHV titres were determined through PCR with reverse transcription (RT–qPCR) following RNA extraction from serum. RNA was extracted from 10 µl of serum using the Pure Viral Nucleic Acid Kit (Roche) and eluted in 30 µl. RT–qPCR was performed following amplification of cDNA reverse transcribed from viral RNA with primers specific for the NS3 region of RHV, TaqMan Fast Virus 1-Step Master Mix for qPCR (Applied Biosystems), and TaqMan QSY Probe (Applied Biosystems). A standard curve was generated using a linearized plasmid encoding the RHV NS3 protein.

Hepatic leukocyte isolation

Isolation of liver-infiltrating leukocytes was performed following perfusion of the liver with PBS through the hepatic portal vein and being passed through 70-µm cell strainers (Fisher). Cells were then isolated via 37% Percoll (Cytiva) gradient density centrifugation at 500*g* for 15 min with slow brake, followed by lysis of residual RBCs in ACK buffer.

Construction and purification of RHV E2 glycoprotein monomer

The purified RHV E2 ectodomain (eE2) monomer was generated as previously described[45]. In brief, an insert containing the RHV E2 ectodomain (amino acids 413–648) upstream of a PreScission protease-cleavable protein A (PA) tag was cloned into the pJG lentiviral vector. Lentiviruses were generated by cotransfecting pJG-RHV E2 with accessory plasmids psPAX2 and pMDG2 into HEK293T cells (purchased from ATCC [CRL-3216] and authenticated and tested negative for mycoplasma by vendor) with Lipofectamine 3000 (Invitrogen). FACSort-purified stable transduction yielded RHV-E2–PA in the supernatant, which was purified by IgG fast flow affinity column (GE Healthcare). The protein A tag was cleaved in-column by PreScission protease (GE Healthcare). Soluble protease was captured by the GSTrap FF column (GE Healthcare) connected in tandem with the IgG FF column before elution of RHV E2.

ELISpot

Total and antigen-specific ASC responses were assessed via spontaneous IgG ELISpot assays without prior cell stimulation. For mouse experiments, plates (Millipore) were directly coated with anti-IgG H+L (Jackson Immuno), RHV eE2 or LCMV NP (provided by R. Ahmed), all in PBS overnight at 4 °C. For human ELISpot, plates were coated with anti-IgG (Mabtech), HCV eE2 (J6, genotype 2a[61]), HBV HBcAg (Prospec), or hepatitis E virus (HEV) protein p239 (provided by Z. Feng). Following blocking, lymphocytes harvested from bone marrow, liver, lymph nodes, spleen and PBMCs were added to ELISpot plates in IMDM (Cytiva HyClone) supplemented with 10% fetal calf serum and 1% penicillin/streptomycin without prior stimulation and left in an incubator with 5% CO_2 at 37 °C overnight. Cryopreserved PBMCs and intrahepatic leukocytes from HCV-infected individuals were thawed and directly plated in the same manner for human ELISpot. Following 16 h of incubation, plates were washed and detected for mouse with anti-Fcγ horseradish peroxidase (HRP) (Jackson) or for human with anti-IgG biotin (Mabtech) and streptavidin-HRP (Mabtech). Plates were developed with ELISpot TMB substrate (Mabtech) for 7 min, quenched and washed with deionized water, and left to dry in the dark overnight until imaging with Immunospot CTL counter and Image Acquisition 4.5 software (Cellular Technology).

ELISA

Serum IgG was determined following the coating of ELISA plates with anti-mouse H+L IgG antibody (Jackson Immuno) at 4 °C overnight. Plates were washed twice and blocked at 37 °C for one hour. Sera was diluted in binding buffer and incubated for 1 h at room temperature. After washing, anti-mouse Fcγ HRP (Jackson Immuno) was then added for 1 h at room temperature. After washing, 50 µl of TMB substrate solution (Thermo) was added prior to quenching with 50 µl of H_2SO_4. Absorbances were read at 450 nm and total IgG concentration was determined from standard curves (Sigma).

Flow cytometry

Leukocytes isolated from various organs were subjected to Fc blocking (Tonbo Biosciences) and subsequently surface stained for 30 min at 4 °C with BV421 anti-CD19 (Biolegend), BV605 anti-CD138 (Biolegend), PE anti-CD38 (BD Biosciences), PE-Cy7 anti-CD95 (BD Biosciences), BUV395 anti-mouse CD4 (BD Biosciences), BV785 anti-CD279 (Biolegend), and biotinylated anti-CXCR5 (Thermo). Cells were then stained with Ghost Dye Violet 510 (Tonbo Biosciences) and streptavidin-APC (Thermo), fixed in Cytofix (BD Biosciences), and washed in FACS buffer prior to acquisition. Data were acquired with BD FACSDiva Software v.9.3.1 and analysed with Flowjo v.10.10.0.

Immunohistochemistry

Liver tissue was fixed in 4% formalin for at least 24 h, embedded in paraffin, and 10-mm sections were cut and placed on charged slides. Sections were dewaxed using xylene and ethanol gradient, followed by heat induced antigen retrieval. Subsequently, the sections were permeabilized in a Triton X–gelatin solution for 20 min, washed 3 times with PBS and blocked with 5% BSA at room temperature for 1 h. Next, the sections were incubated for 1 h with anti-mouse IgG at room temperature. Afterward, the slides were washed in PBS and mounted using a DAPI-containing mounting medium. Images were captured using a Nikon A1RHD confocal microscope at Emory University.

BCR sequencing

For BCR sequencing, whole organs were first lysed and digested in RLT using TissueRuptor (Qiagen), followed by RNA extraction with RNeasy Mini Extraction Kit (Qiagen). Samples were amplified using iR-RepSeq+ Mouse BCR IgH primers from a total RNA input of 1,200 ng. Next-generation sequencing libraries were generated encompassing the BCR heavy chain with unique molecular identifiers being incorporated during the reverse transcription step and first-strand cDNA selection with removal of remnant primers via SPRIselect bead purification (Beckman Coulter). After 2 additional rounds of amplification and purification, libraries were multiplexed and sequenced on 10% of a Nextseq 1000 P1 600 cycle. Sequencing data were analysed using the iRmap program[62,63]. In brief, Ig heavy chain (IgH) sequence reads were de-multiplexed and compared to an IMGT reference library[64] for mapping to germline V, D, J and C sequences. For generation of clonal lineage trees, representative IgH sequences of expanded BCR clones were selected for clonal lineage analysis. Phylogenetic trees were created using IgPhyml from the immcantation framework (v.4.0.0)[65,66] and plotted using the alakazam R library[67] with unique CDR3 nodes being defined by a hamming distance of one.

Visium HD spatial transcriptomics

Spatial transcriptomic libraries were generated using the Visium HD Spatial Gene Expression Reagent Kit (10x Genomics, PN-1000668) according to the manufacturer's instructions at UAB Flow Cytometry and Single Cell Core. First, the FFPE tissues were assessed for RNA quality and the samples with DV200 >50% were selected for the assay. In brief, the tissue slides were prepared with 5-µm sections at the UAB Comparative Pathology Lab and were subjected to H&E staining. The 6.5 mm × 6.5 mm ROIs were imaged at 20× magnification using a Lionheart FX (Biotek) at the UAB High Resolution Imaging Facility. The tissue sections were then decrosslinked and hybridized with Visium Mouse Transcriptome Probes v.2. The hybridized probes were captured by the Visium HD Slide oligos using the CytAssist instrument (10x Genomics), amplified, and the final sequencing libraries were generated. The libraries were subjected to 2× 150 bp pair-end sequencing with a sequencing depth of 275 million reads per sample on an Illumina NovaSeq plus instrument (Azenta Life Sciences). Demultiplexing and sequence analysis, along with alignment to H&E-stained images, were carried out using the SpaceRanger pipeline. Individual transcript localization, graph-based clustering, and clustered gene expression heat maps were generated in Loupe Browser v.8.0.0. Graph-based clusters were subjected to manual annotation and cross-validated with ACT[68] and PanglaoDB[69] cell annotation databases.

Xenium Prime spatial transcriptomics

FFPE tissue sections from mouse and human liver samples were arranged into tissue microarrays from H&E-stained samples and 5-µm sections were mounted onto Xenium slides at Acepix Biosciences. Such arrays of 8 tissue cores (4 mm diameter each) were arranged to fit within the 12 × 24 mm designated slide area. These slides were processed using the Xenium In Situ platform (10x Genomics) at UAB Flow Cytometry and Single Cell Core following the manufacturer's protocol. In brief, the samples were probe hybridized with the Xenium Prime 5K Mouse/Human Pan Tissue and Pathways panel, along with custom panels of 100 additional genes each, based on rational selection and design. Following probe hybridization, ligation and rolling circle amplification, the Xenium cell segmentation cocktail for morphology-based cell partition was also included in the workflow. The slides were then loaded onto the Xenium analyser instrument for automated imaging and signal decoding. Transcript assignments, segmented cell boundaries, and unsupervised clustering were performed in the instrument by Xenium Onboard Analysis software and visualized using Xenium Explorer v.3.2. Objective selection criteria for intrahepatic leukocytic aggregates in human liver tissue required all of the following: transcript density for *LTB* $\geq 4 \times 10^{-4}$, *MS4A1* or *CD4* $\geq 4 \times 10^{-3}$, *CXCL13* $\geq 3 \times 10^{-4}$ and *CCL19* $\geq 10^{-3}$ and total transcript count of *LTB* ≥10 and *MS4A1* or *CD4* ≥50. Downstream analyses were conducted in Xenium Explorer 3 with manual cell-type annotation of individually segmented cells utilizing ACT[68] and PanglaoDB[69] cell annotation databases.

Statistical analyses

Statistical analyses were performed with Prism v.10 (GraphPad). Specific tests used are provided in each figure legend. Statistical significance was denoted as indicated: $^{*}P \leq 0.05$, $^{**}P \leq 0.01$, $^{***}P \leq 0.001$ and $^{****}P \leq 0.0001$.

Obtaining biological materials

Biological materials used in this study can be made available to the scientific community by directly contacting the corresponding author.

Reporting summary

Further information on research design is available in the Nature Portfolio Reporting Summary linked to this article.

Data availability

The data supporting the findings of this study are available in the article. Mouse BCR sequencing data are located at https://doi.org/10.5281/zenodo.17345590 (ref. 70), mouse spatial transcriptomics data are located at https://doi.org/10.5281/zenodo.17346168 (ref. 71), and human spatial transcriptomics data are located at https://doi.org/10.5281/zenodo.17354774 (ref. 72). Source data are provided with this paper.

61. Boisvert, M. et al. Novel E2 glycoprotein tetramer detects hepatitis C virus-specific memory B cells. *J. Immunol.* **197**, 4848–4858 (2016).
62. Wang, C. et al. High throughput sequencing reveals a complex pattern of dynamic interrelationships among human T cell subsets. *Proc. Natl Acad. Sci. USA* **107**, 1518–1523 (2010).
63. Yang, Y. et al. Distinct mechanisms define murine B cell lineage immunoglobulin heavy chain (IgH) repertoires. *Elife* **4**, e09083 (2015).

64. Lefranc, M. P. et al. IMGT, the international ImMunoGeneTics information system. *Nucleic Acids Res.* **37**, D1006–D1012 (2009).
65. Hoehn, K. B. et al. Repertoire-wide phylogenetic models of B cell molecular evolution reveal evolutionary signatures of aging and vaccination. *Proc. Natl Acad. Sci. USA* **116**, 22664–22672 (2019).
66. Hoehn, K. B., Lunter, G. & Pybus, O. G. A phylogenetic codon substitution model for antibody lineages. *Genetics* **206**, 417–427 (2017).
67. Gupta, N. T. et al. Change-O: a toolkit for analyzing large-scale B cell immunoglobulin repertoire sequencing data. *Bioinformatics* **31**, 3356–3358 (2015).
68. Quan, F. et al. Annotation of cell types (ACT): a convenient web server for cell type annotation. *Genome Med.* **15**, 91 (2023).
69. Franzén, O., Gan, L. M. & Björkegren, J. L. M. PanglaoDB: a web server for exploration of mouse and human single-cell RNA sequencing data. *Database* https://doi.org/10.1093/database/baz046 (2019).
70. Gridley, J. et al. BCR IGH sequencing for: iHALT unlocks liver functionality as a surrogate secondary lymphoid organ [Data set]. *Zenodo* https://doi.org/10.5281/zenodo.17345590 (2025).
71. Gridley, J. et al. Mouse spatial transcriptomics data for: iHALT unlocks liver functionality as a surrogate secondary lymphoid organ [Data set]. *Zenodo* https://doi.org/10.5281/zenodo.17346168 (2025).
72. Gridley, J. et al. Human spatial transcriptomics data for: iHALT unlocks liver functionality as a surrogate secondary lymphoid organ [Data set]. *Zenodo* https://doi.org/10.5281/zenodo.17354774 (2025).

Acknowledgements We thank J. Jacob, Z. Feng and R. Ahmed for providing valuable reagents; E. Elrod, A. Pradhan, S. Watry and N. Pazira for technical assistance; J. Magliocca, D. J. Lo, S. Kim, M. Kazimi and F. Siddiqui for providing liver samples, along with the nursing staff and consenting team members; S. Liu, C.-W. Sun, M. Basu, E. Dessasau, K.-J. Chang, P. Laaguiby, R. Mote, J. Brown, W. Pan, B. Brown, D. Weber, K. Gill, A. Saini and Emory University Integrated Cellular Imagining Core Facility (RRID:SCR_023534); and the veterinary and animal care staff of Emory National Primate Research Center for their assistance. This project was supported by NIH grants R01AI136533 and U19AI159819 to A.G., ORIP/OD P51OD011132 (formerly NCRR P51RR000165) to the Emory National Primate Research Center (A.G.), R01AI151175 and R01AI183877 (A.G. and A. Kapoor), and R01AI185926 (A. Kapoor). J.G. was supported by Emory Vaccinology Training grant T32 5T32AI074492-14 and NIAID F32 fellowship award F32AI189066. The content is solely the responsibility of the authors and does not necessarily represent the official views of the National Institutes of Health.

Author contributions J.G. conceived and designed the study, carried out experiments, analysed and interpreted data, and wrote the manuscript. D.P. conceived and designed the study, carried out experiments, and analysed and interpreted data. A. Kumari, J.S., B.H., Y.S., S.T. and Y.W. assisted with experiments, and analysed and interpreted data. S.P.K. helped design the study and provided intellectual input. A. Kapoor and R.T.C. analysed and interpreted data and provided intellectual input. A.G. conceived and designed the study, analysed and interpreted data, acquired funding, and wrote the manuscript, with all authors contributing to writing and providing feedback.

Competing interests The authors declare no competing interests.

Additional information

Supplementary information The online version contains supplementary material available at https://doi.org/10.1038/s41586-025-09803-4.

Correspondence and requests for materials should be addressed to Arash Grakoui.

Peer review information *Nature* thanks Antonio Bertoletti, Percy Knolle, Nina Le Bert, Robert Thimme and the other, anonymous, reviewer(s) for their contribution to the peer review of this work.

Reprints and permissions information is available at http://www.nature.com/reprints.

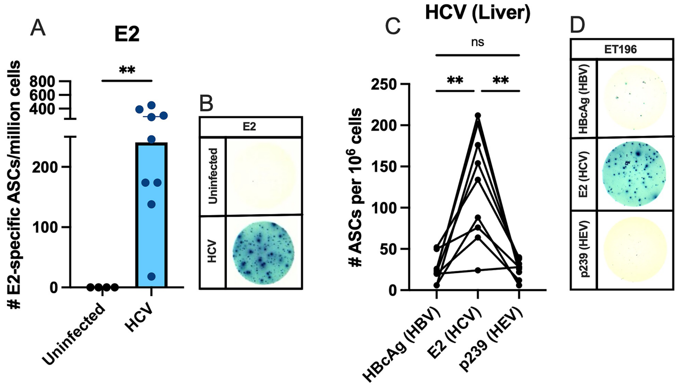

Extended Data Fig. 1 | Uninfected human liver samples do not have cross-reactive E2-specific ASCs and intrahepatic ASCs in HCV-infected humans demonstrate high specificity for E2. Intrahepatic leukocytes were incubated overnight without prior stimulation on plates coated with respectively labeled antigens demonstrating (A) lack of E2-specific ASCs in uninfected human liver samples and (C) specificity for E2 over other irrelevant proteins. Representative ELISpot images are shown from liver samples of (B) uninfected and HCV-infected humans as well as (D) from an HCV-infected donor (ET196). (A) Mean + SEM. Statistical tests performed were (A) two-tailed, unpaired t-test and (C) one-way ANOVA with Tukey's multiple comparisons test. (A) $p = 0.0045$, (C) HBcAg vs. p239: $p = 0.9896$, HBcAg vs. E2: $p = 0.0059$, E2 vs. p239: $p = 0.0038$. Statistical significance was denoted as $** = (p \leq 0.01)$.

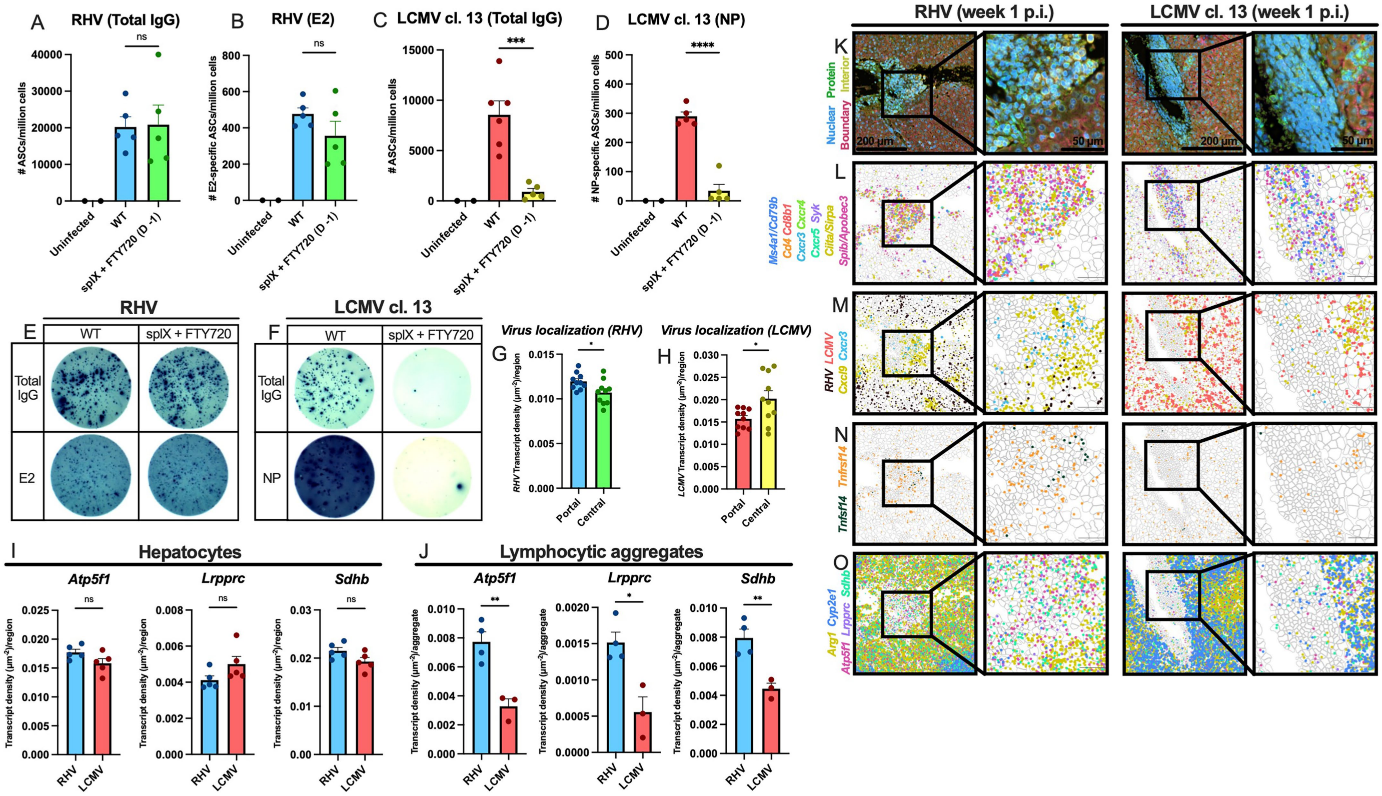

Extended Data Fig. 2 | Systemic infection of prolonged duration still does not induce locally generated humoral immunity and harbors virus and immature leukocyte aggregates confined to zone 3 with marked reduction of oxidative phosphorylation compared to early iHALT precursors. (A, C) Total and (B, D) virus-specific ASCs were quantified in the liver at week 4 post-infection for (A, B) RHV and (C, D) LCMV clone 13 infection with (E, F) representative ELISpot images showing (A, B) representative and (C, D) pooled data from (A-D) n = 2 independent experiments. Mice were either untreated (WT) or splenectomized and treated with FTY720 prior to infection with treatment being maintained throughout (splX + FTY720 [D -1]). Virus localization was determined by viral transcript density for individual portal and central zones at week 1 post-infection during (G) RHV and (H) LCMV clone 13 infection from n = 10 portal and n = 10 central zone selections from a Xenium 5 K spatial transcriptomics run of n = 1 mouse liver per group. Transcript density of genes associated with oxidative phosphorylation usage were quantified in (I) portal zone hepatocyte regions and (J) immature lymphocytic clusters at week 1 post-infection. Following (K) upstream staining, (L-O) individual transcript localization was determined in the liver at week 1 post-infection. (A-D, G-J) Mean + SEM. (A-D, G-J) Two-tailed, unpaired t-tests were performed. (A) p = 0.9168, (B) p = 0.1987, (C) p = 0.0008, (D) p < 0.0001, (G) p = 0.0261, (H) p = 0.0282. Statistical significance was denoted as *=(p ≤ 0.05), **=(p ≤ 0.01), ***=(p ≤ 0.001), and ****=(p ≤ 0.0001).

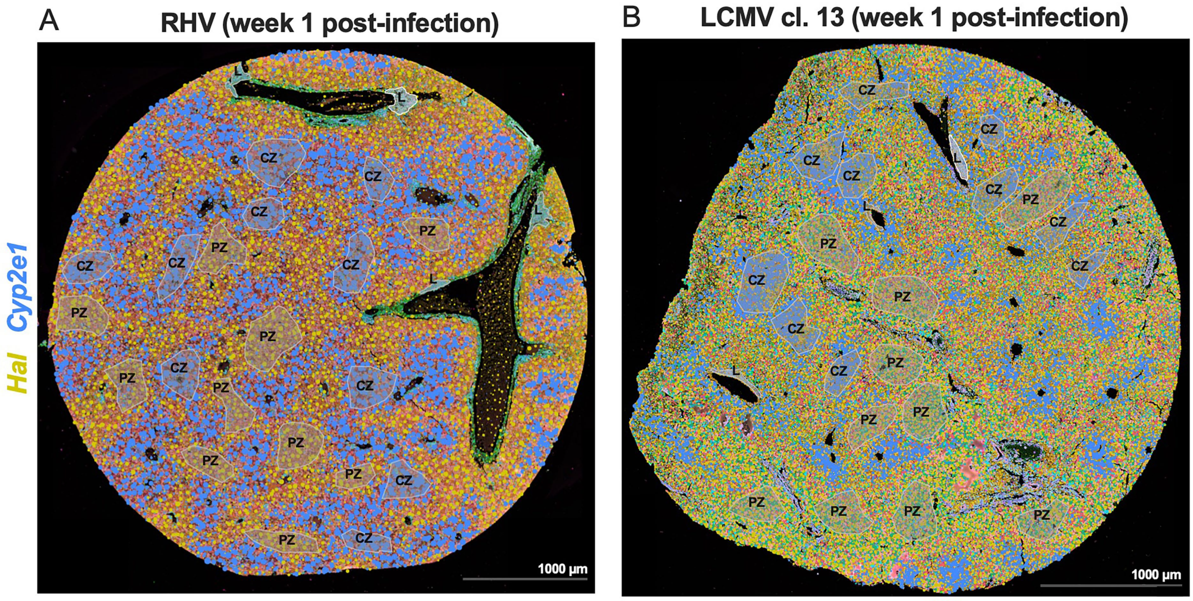

Extended Data Fig. 3 | Selection of intrahepatic portal and central zones. (A, B) Portal and central zones used for quantification of various transcripts (Extended Data Fig. 4) were selected based on expression of various zone-specific transcripts, such as *Hal* (portal) and *Cyp2e1* (central) at week 1 post-infection with either (A) RHV or (B) LCMV clone 13 infection.

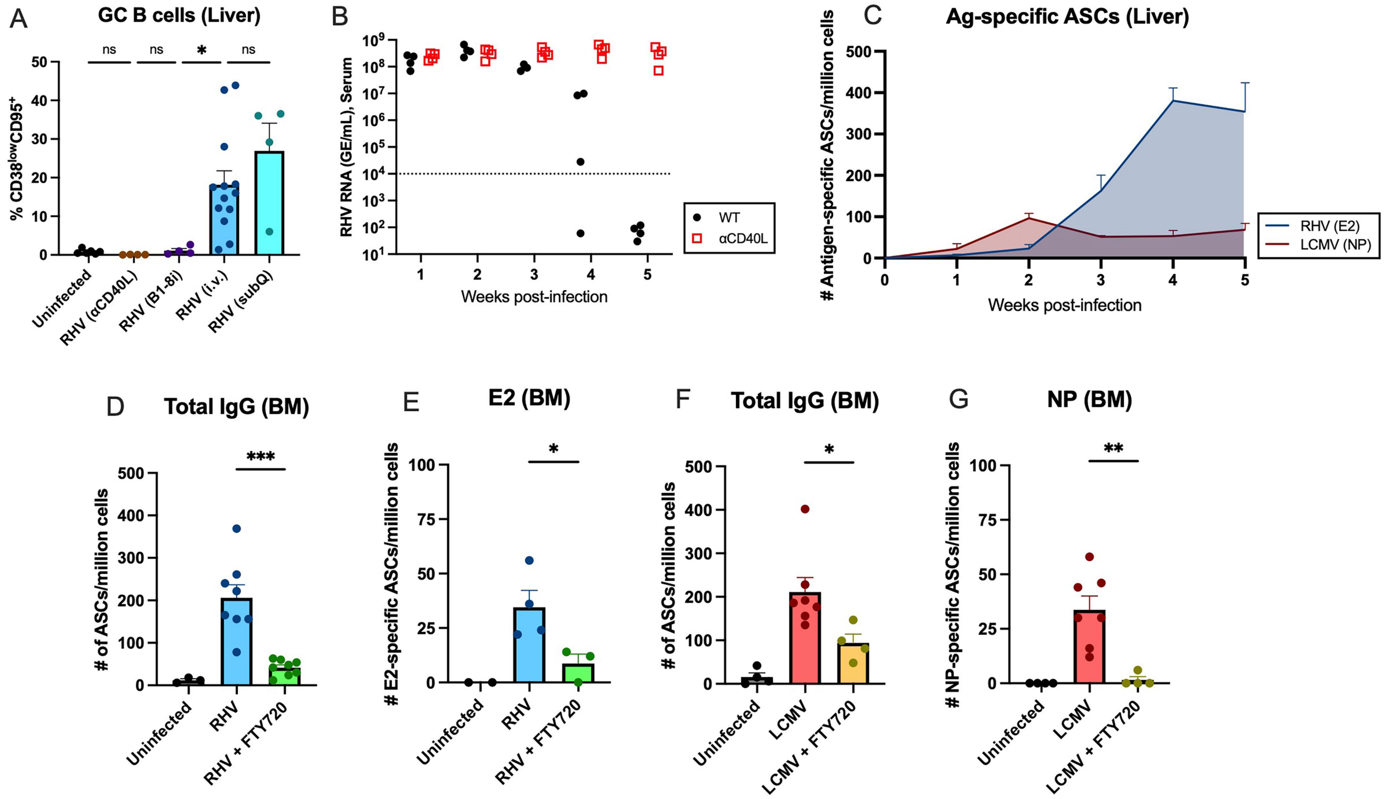

Extended Data Fig. 4 | Humoral dynamics during RHV and LCMV infection. (A) CD38^{low}CD95^{+} GC-like B cell frequency in the liver is shown at 4 weeks post-RHV infection for uninfected controls, mice treated with αCD40L beginning at day 11 post-infection onwards three times weekly, BCR-restricted B1-8i mice, and WT mice infected either intravenously or subcutaneously. (B) RHV serum viremia is shown for WT mice that were untreated or treated with αCD40L three times weekly beginning at day 11 post-infection. (C) Mean + SEM intrahepatic antigen-specific ASCs were shown kinetically throughout RHV (blue) and LCMV (red) infection. Total (D, F) and antigen-specific (E, G) ASCs were shown in the bone marrow at 4 weeks post-infection with RHV (D, E) or LCMV (F, G) infection with or without FTY720 treatment beginning at day -1 prior to infection and being maintained throughout thereafter three times weekly. (A, C-G) Mean + SEM. (A, C-G) Statistical tests performed were (A) one-way ANOVA with Tukey's multiple comparisons test and (D-G) two tailed, unpaired t-test. (A) $p = 0.0498$, (D) $p = 0.0001$, (E) $p = 0.0482$, (F) $p = 0.0375$, (G) $p = 0.0045$. Statistical significance was denoted as *=($p \leq 0.05$), **=($p \leq 0.01$), and ***=($p \leq 0.001$).

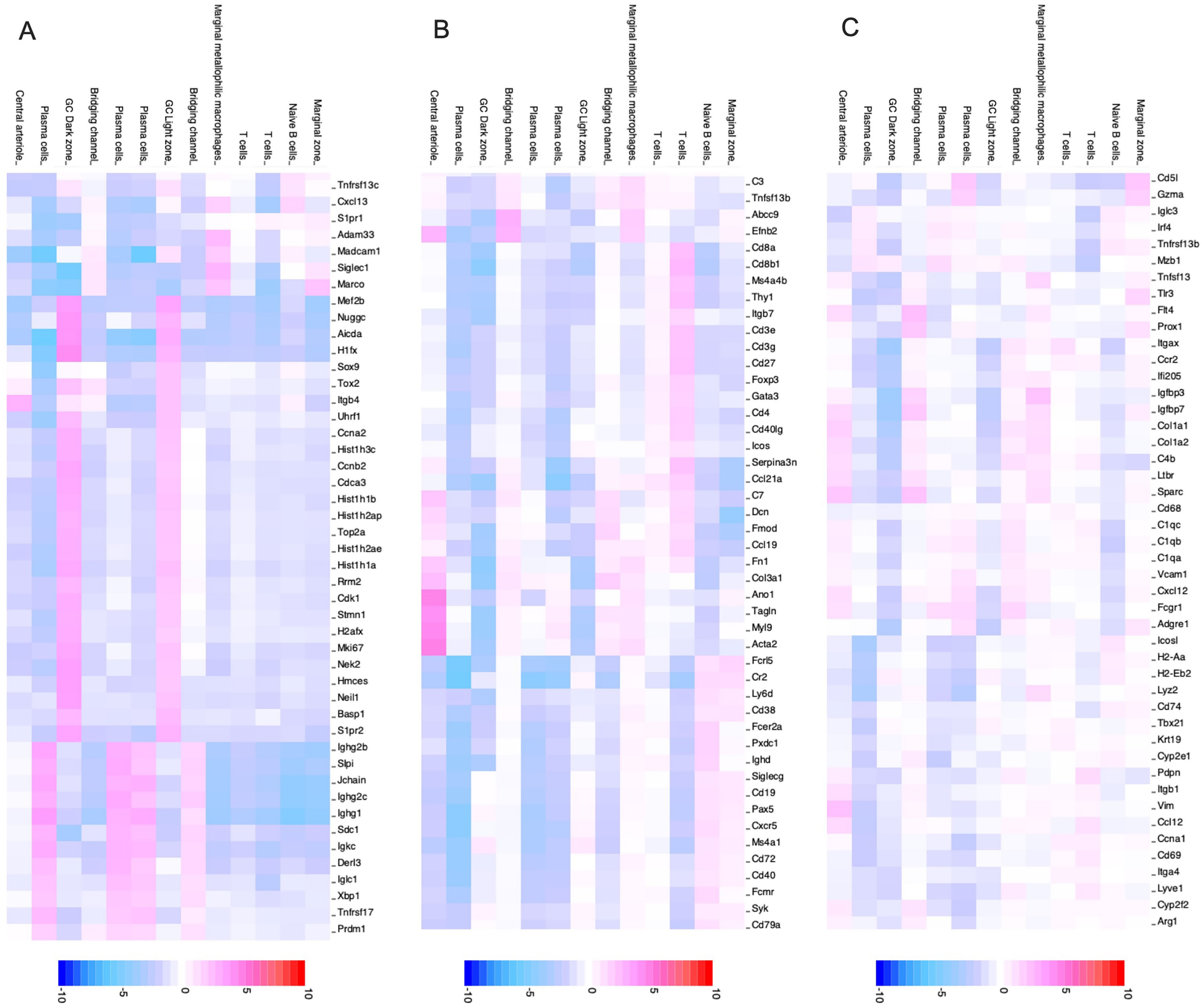

Extended Data Fig. 5 | Spatial transcriptomic clustering of Visium HD annotated clusters in the spleen following LCMV infection. (A-C) Individual transcripts added to Feature List were scaled as heatmaps of graph-based clusters generated in Loupe Browser v8.0.0. Annotated clusters corresponding to Fig. 3i are shown at 4 weeks post-infection with LCMV in the spleen.

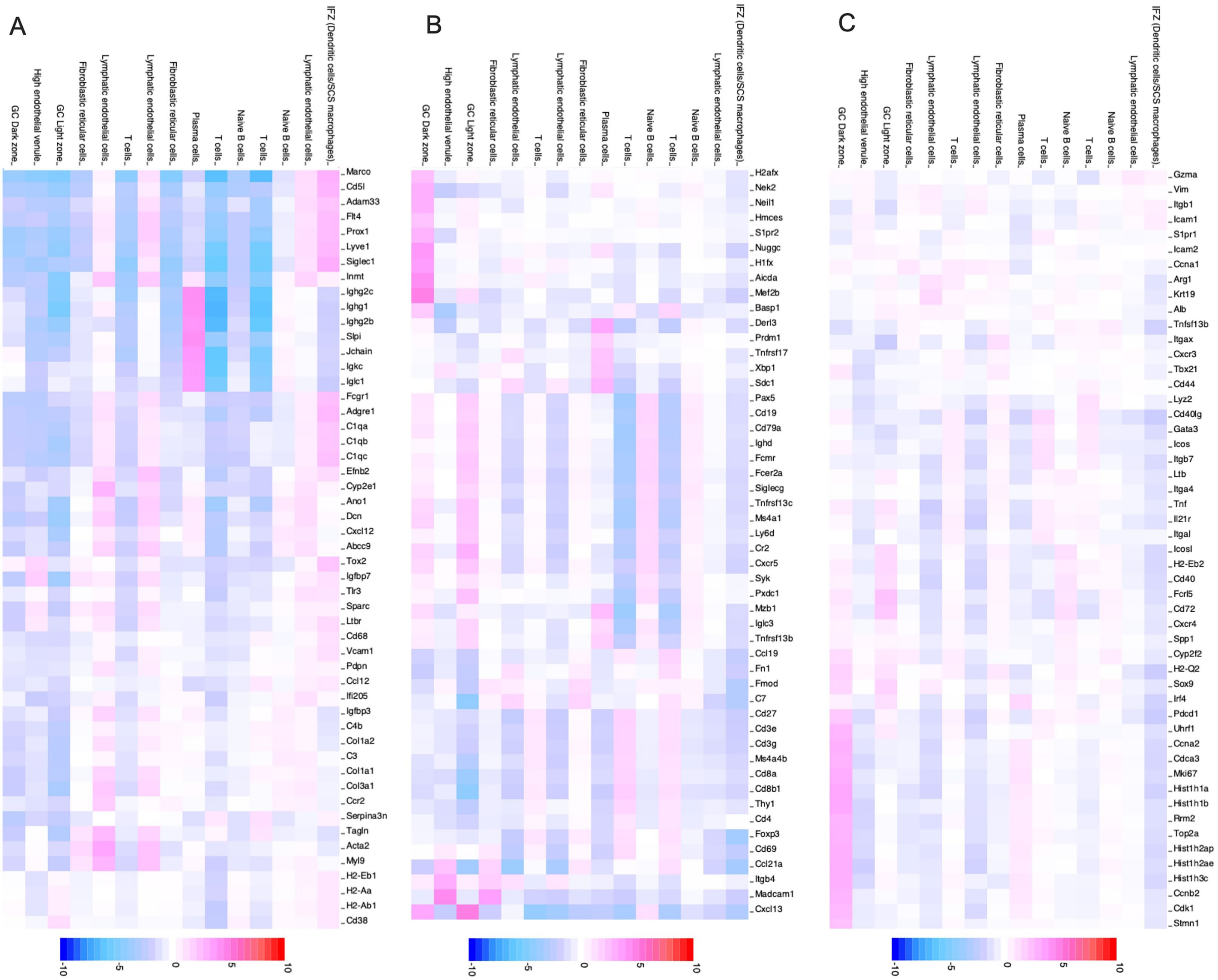

Extended Data Fig. 6 | Spatial transcriptomic clustering of Visium HD annotated clusters in the mesenteric lymph nodes following LCMV infection. (A-C) Individual transcripts added to Feature List were scaled as heatmaps of graph-based clusters generated in Loupe Browser v8.0.0. Annotated clusters corresponding to Fig. 3i are shown at 4 weeks post-infection with LCMV in the mesenteric lymph nodes.

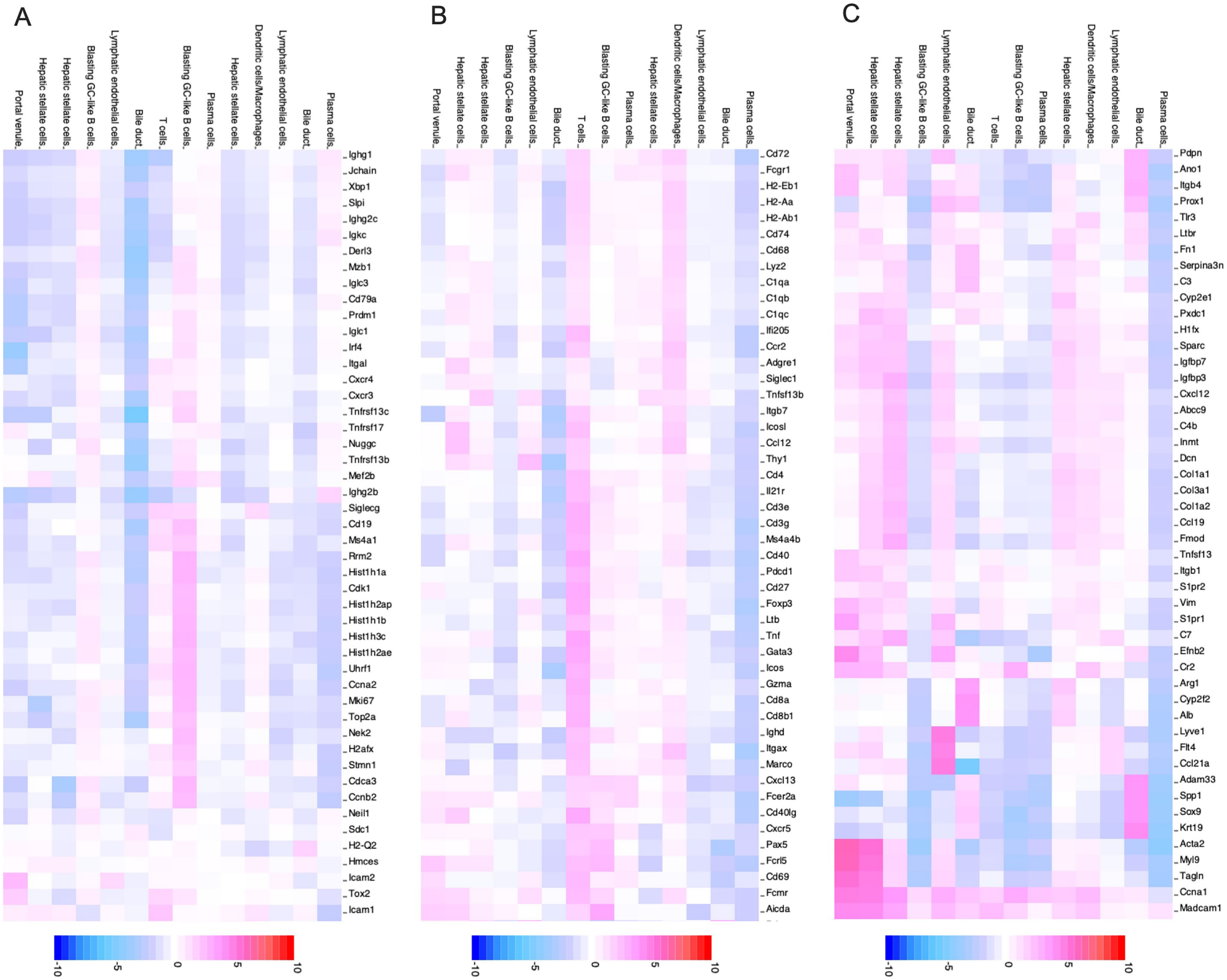

Extended Data Fig. 7 | Spatial transcriptomic clustering of Visium HD annotated clusters in the liver following RHV infection. (A-C) Individual transcripts added to the Feature List were scaled as heatmaps of graph-based clusters generated in Loupe Browser v8.0.0. Annotated clusters corresponding to Fig. 3i are shown at 4 weeks post-infection with RHV in the liver.

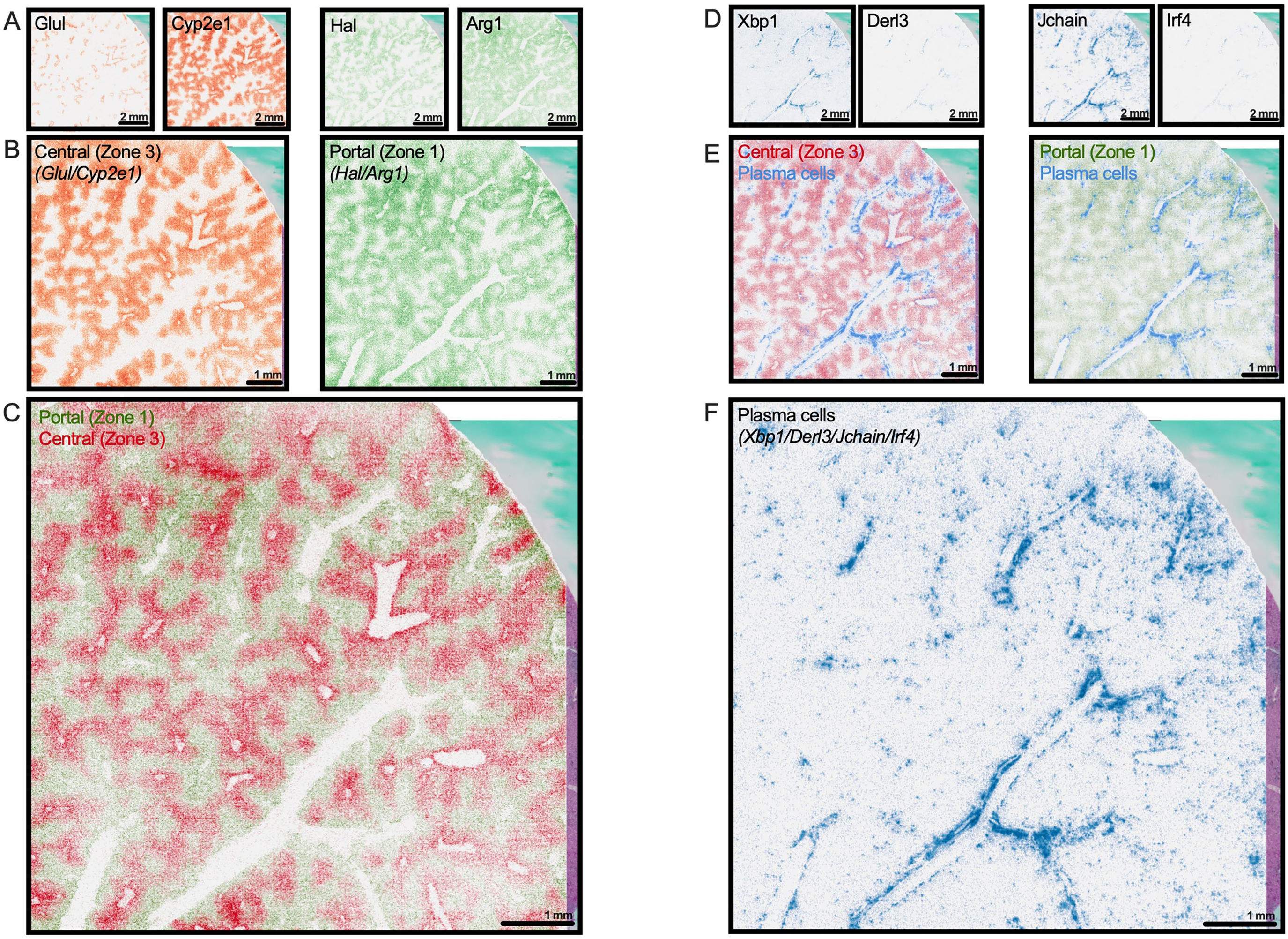

Extended Data Fig. 8 | Plasma cell localization during strictly hepatotropic viral infection is primarily confined to periportal zone 1 of the liver and absent near central veins. (A-F) Visium HD spatial transcriptomic outputs at 4 weeks post-RHV infection in the liver displayed as log2-scaled heatmaps of 8 µm bins for single-parameter panels and feature sums for multiple-parameter lists. (A) Transcripts characteristic of central zone (zone 3) are shown in orange (*Glul, Cyp2e1*) while those characteristic of portal zone (zone 1) are shown in green (*Hal, Arg1*). (B) Co-expression of central (orange) and portal (green) zone-related transcripts shown in (A) as combined feature sums. (C) Merged expression of central (red, *Glul* and *Cyp2e1*) and portal (green, *Hal* and *Arg1*) combined transcripts. (D) Expression of various plasma cell-related transcripts as shown in blue (*Xbp1*, *Derlr3*, *Jchain*, *Irf4*). (E) Merged expression of transcripts indicative of the central zone (red, *Glul* and *Cyp2e1*) and plasma cells (*Xbp1*, *Derl3*, *Jchain*, *Irf4*). (F) Merged expression of transcripts indicative of the portal zone (green, *Hal* and *Arg1*) and plasma cells (*Xbp1*, *Derl3*, *Jchain*, *Irf4*). (F) Co-expression of plasma cell-related transcripts (*Xbp1*, *Derl3*, *Jchain*, *Irf4*) as feature sum list. (A, F) From morphologically similar H&E staining with limited interindividual variability conducted on n = 5 mice, data is shown from n = 1 mouse liver tissue with which Visium HD spatial transcriptomics was conducted.

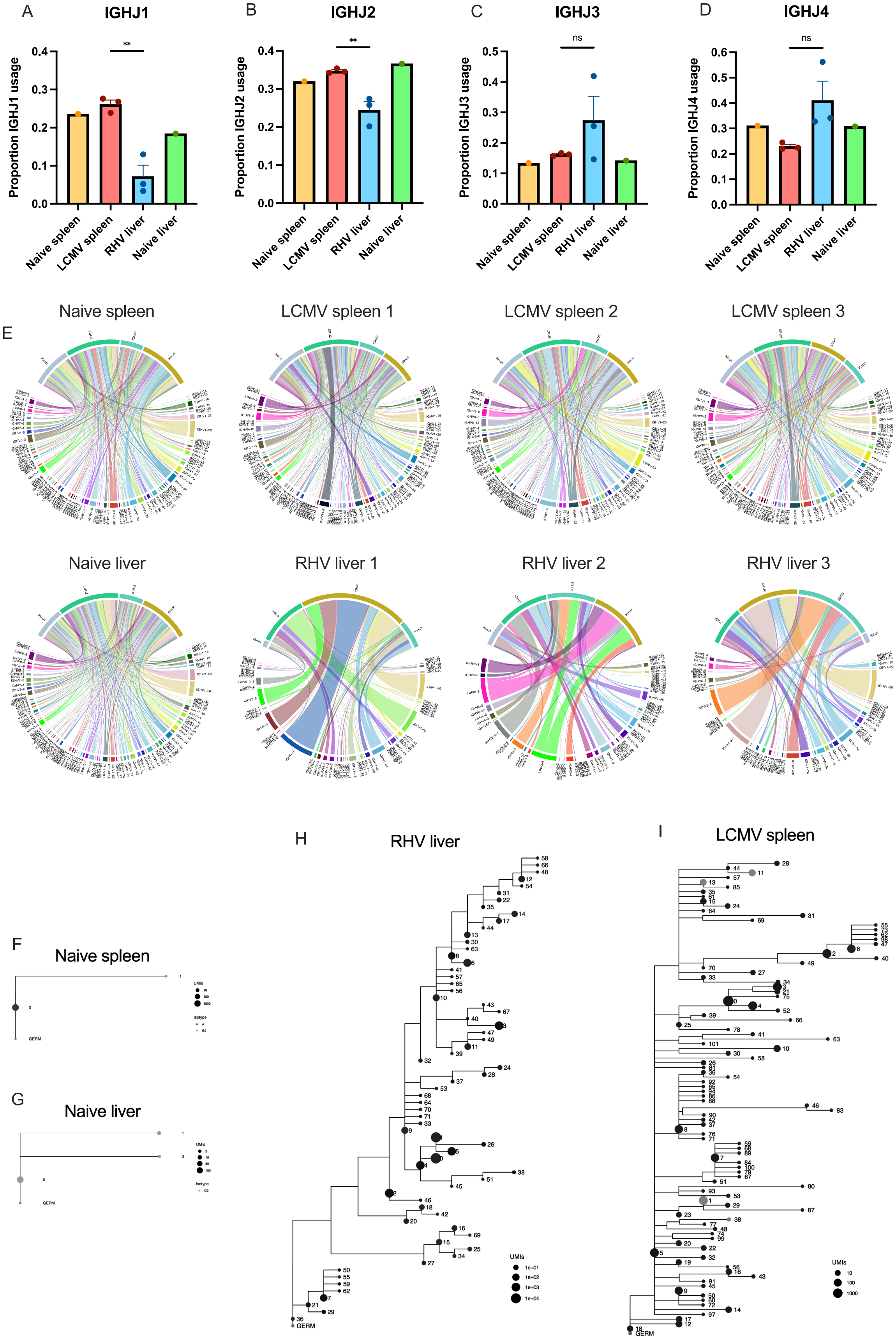

Extended Data Fig. 9 | See next page for caption.

Extended Data Fig. 9 | Strictly hepatotropic viral infection induces iHALT with oligoclonal expansion and comparable levels of SHM compared to the spleen during systemic infection. (A-D) Proportion of IGHJ gene family usage in n = 1 naïve spleen, n = 3 LCMV-infected spleens (week 4 post-infection), n = 3 RHV-infected livers (week 4 post-infection), and n = 1 naïve liver with (A-D) two-tailed, unpaired t-tests. (E) Chord diagrams representing IgH V-J gene family pairing. Representative clonal lineage trees displaying nucleotide divergence from germline clones obtained from (F) naïve spleen, (G) naïve liver, (H) RHV-infected liver, and (I) LCMV-infected spleen. (A-D) Mean + SEM. (A-D) Two-tailed, unpaired t-tests were performed for LCMV spleen vs. RHV liver. For (A-D) LCMV spleen vs. RHV liver: (A) $p = 0.0039$, (B) $p = 0.0099$, (C) $p = 0.2334$, (D) $p = 0.0780$. Statistical significance was denoted as **=($p \le 0.01$).

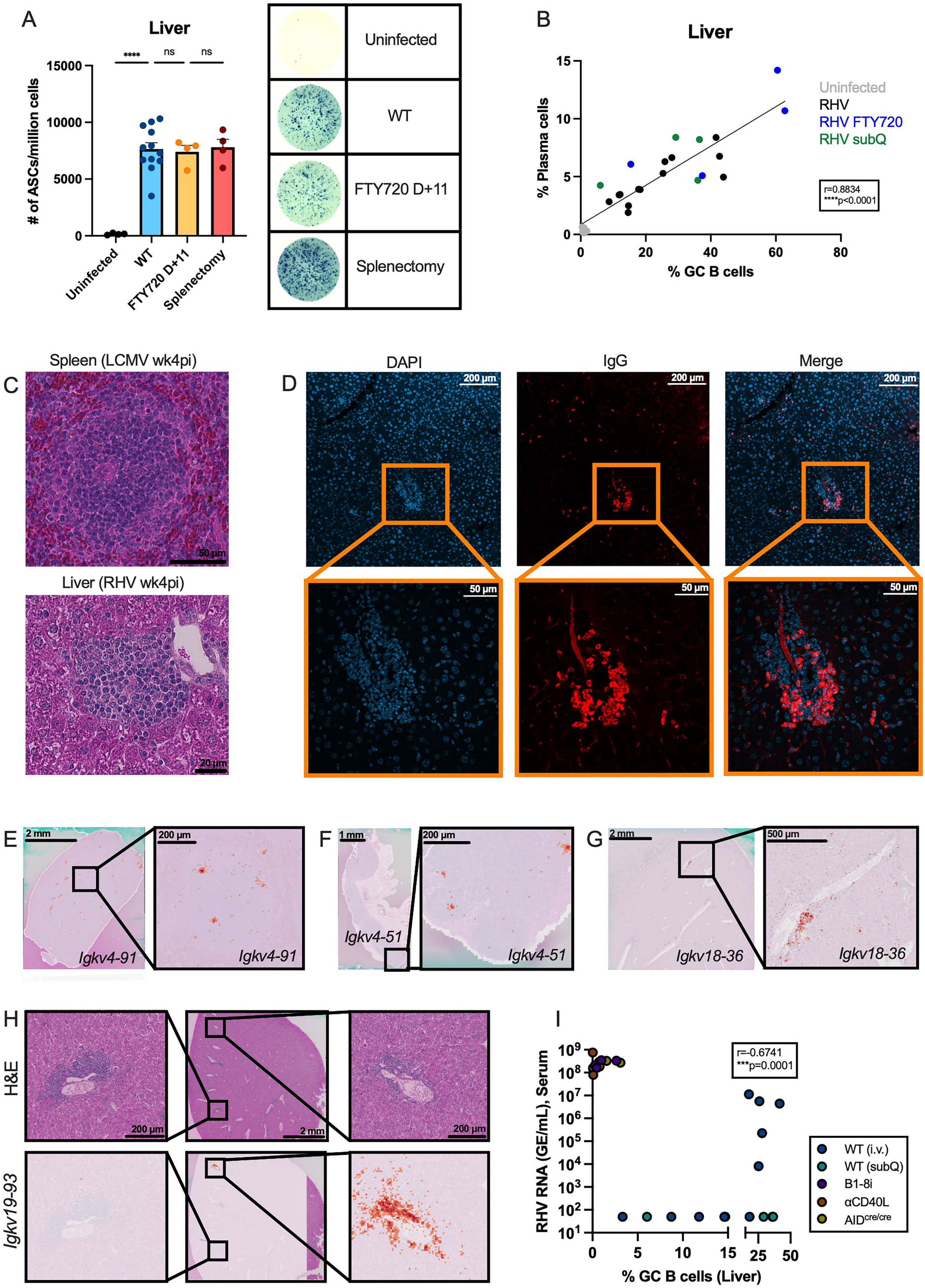

Extended Data Fig. 10 | See next page for caption.

Extended Data Fig. 10 | iHALT is unhindered by splenectomy, exhibits polarized IgG$^+$ cell localization, and harbors isolated BCR clonal distribution. (A) Number of total IgG$^+$ ASCs in the liver at week 4 post-RHV infection following splenectomy one week prior to infection or FTY720 administration beginning at day 11 post-infection onward with representative ELISpot image. (B) Correlation between % plasma cells (CD38^{low}CD138$^+$ of total B cells) and % GC B cells (CD38^{low}CD95$^+$ of total B cells) in the liver at 4 weeks post-infection with RHV. (C) Representative H&E staining of FFPE sections from spleen at week 4 post-LCMV infection and liver at week 4 post-RHV infection. (D) Immunofluorescence staining of FFPE sections at 4 weeks post-RHV infection. Localization of representative Ig kappa gene families displayed as log2-scaled heatmaps of 8 µm bins at 4 weeks post-infection in (E) spleen (LCMV), (F) mesenteric lymph nodes (LCMV) and (G) liver (RHV). (H) From liver tissue at 4 weeks post-infection with RHV following FTY720 treatment, H&E (top) is shown for corresponding ROIs where *Igkv19–93* localization is shown as log2-scaled heatmaps of 8 µm bins (bottom). (I) Correlation between intrahepatic CD38^{low}CD95$^+$ GC B cells and RHV serum viremia at 4 weeks post-infection. (A-B) Data shown are representative or pooled values from 2-3 independent experiments of 3–9 mice per group. Visium HD spatial transcriptomics was conducted with liver tissue from n = 1 representative mouse following similar H&E morphological staining with limited interindividual variability from (C) n = 4 (spleen) and n = 4 (liver), (E) n = 4, (F) n = 4, (G) n = 5, and (H) n = 4 mice. (D) Representative image shown from immunofluorescent staining that was performed with liver tissue from n = 4 mice. (A) Mean + SEM. Statistical tests performed were (A) one-way ANOVA with Tukey's multiple comparisons test and (B, I) two-tailed nonparametric Spearman correlation with Pearson's *r* coefficient. (A) Uninfected vs. WT: $p < 0.0001$, WT vs. FTY720 D + 11: $p = 0.9939$, FTY720 D + 11 vs. Splenectomy: $p = 0.9853$. Statistical significance was denoted as ****=($p \leq 0.0001$).

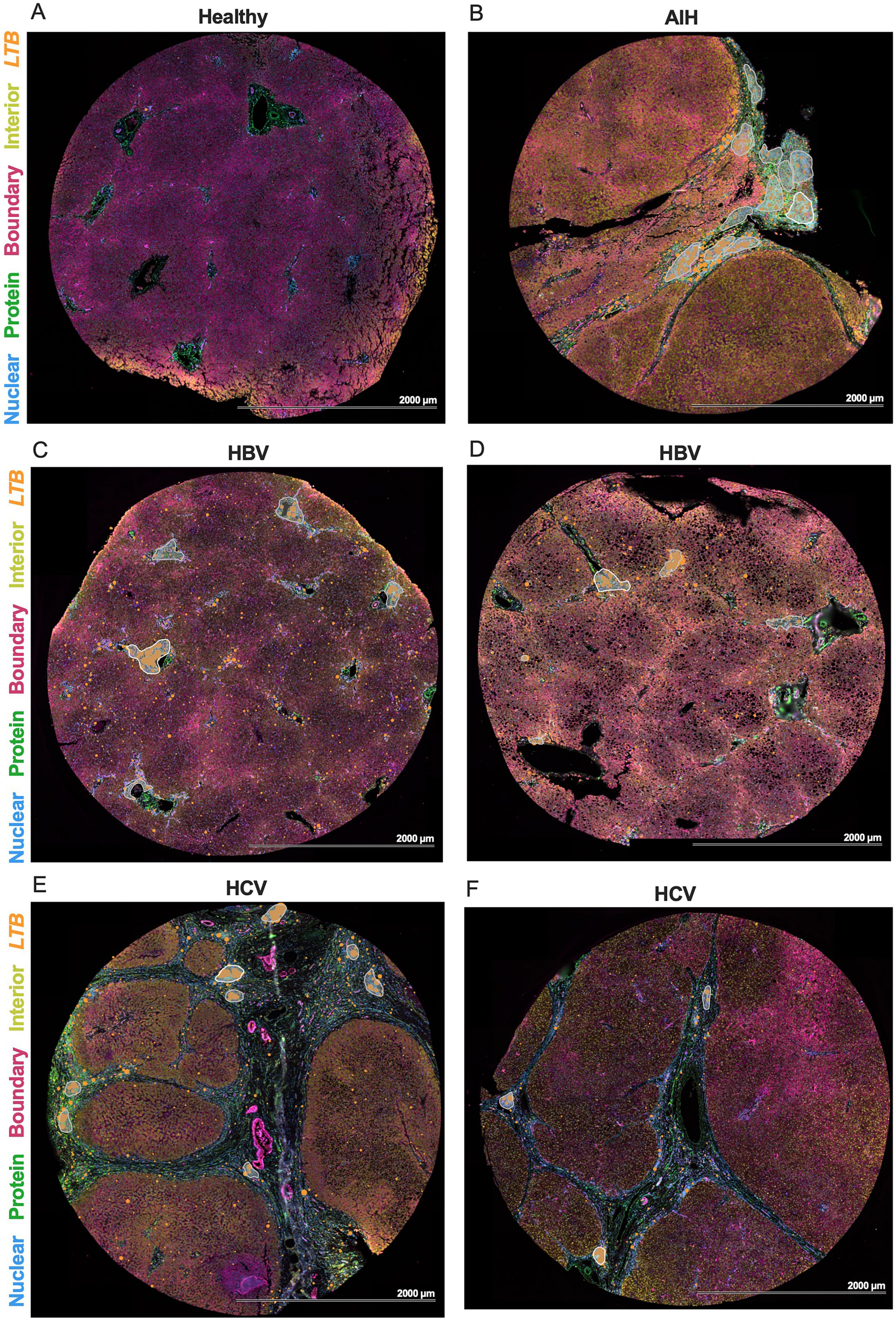

Extended Data Fig. 11 | Selection of intrahepatic lymphoid aggregates in human liver tissue. (A-F) For various labeled liver conditions, intrahepatic lymphoid aggregate selections utilized for downstream analysis (Fig. 5) were made based all of the following criteria being met: transcript density of *LTB* $\geq 4e^{-4}$, *MS4A1* or *CD4* $\geq 4e^{-3}$, *CXCL13* $\geq 3e^{-4}$ or *CCL19* $\geq 1e^{-3}$ and total transcript count of *LTB* ≥ 10, *MS4A1* or *CD4* ≥ 50.

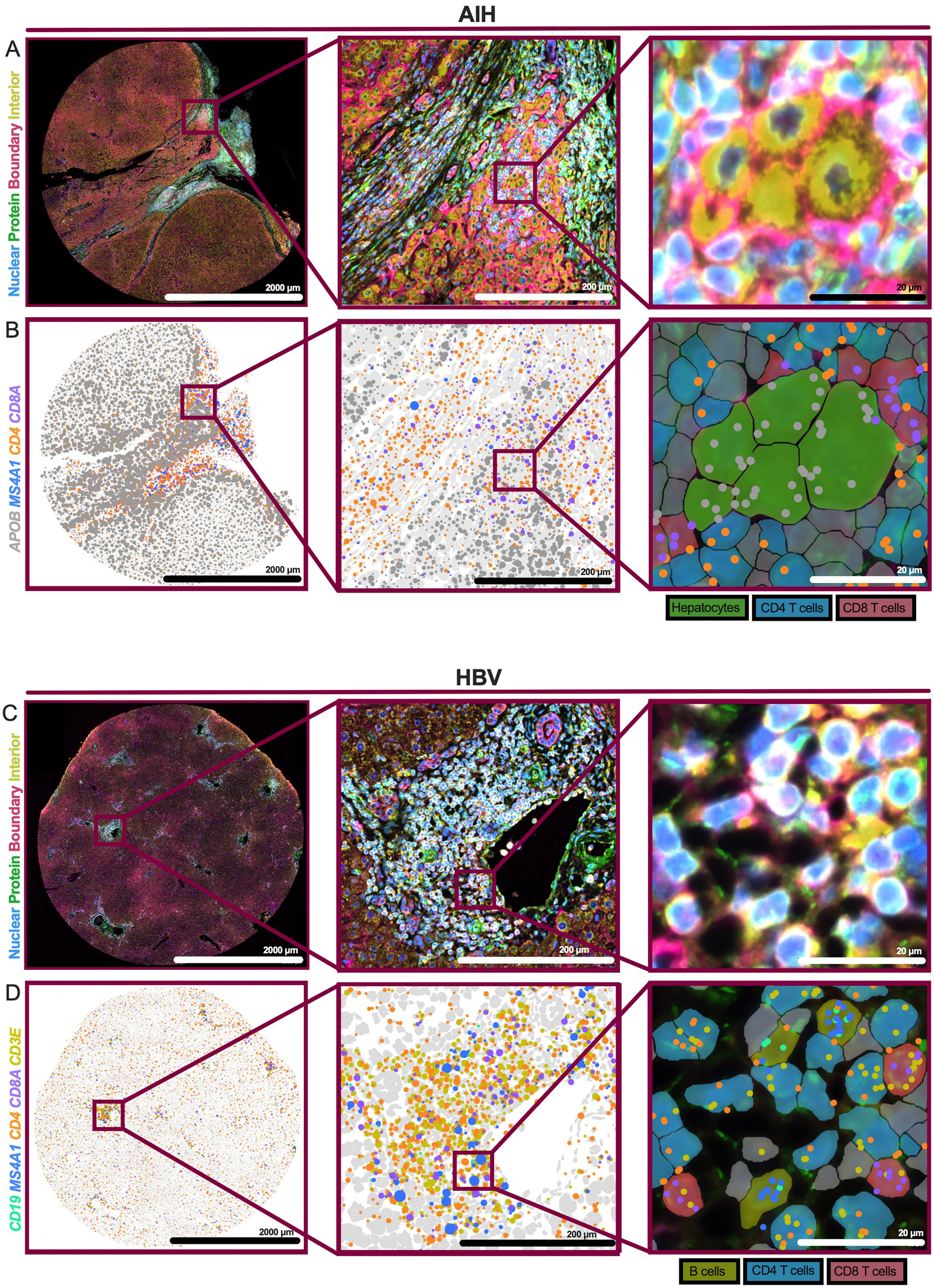

Extended Data Fig. 12 | See next page for caption.

Extended Data Fig. 12 | Spatial transcriptomic characterization of intrahepatic lymphoid aggregates in human AIH and HBV infection. Xenium Prime 5 K spatial transcriptomics was performed with liver tissue obtained during human (A, B) AIH and (C, D) HBV infection. Depicted are regions of interest showing (A, C) upstream morphological staining and (B, D) expression of various color-coded transcripts and annotated cell types. Data shown from (A, B) n = 1 individual with AIH and (C, D) n = 1 individual chronically infected with HBV from which liver tissue was selected for spatial transcriptomics conducted on (A, B) n = 1 individual and (C, D) n = 2 individuals with limited interindividual variability.

nature portfolio

Corresponding author(s): Arash Grakoui
Last updated by author(s): Oct 15, 2025

Reporting Summary

Nature Portfolio wishes to improve the reproducibility of the work that we publish. This form provides structure for consistency and transparency in reporting. For further information on Nature Portfolio policies, see our Editorial Policies and the Editorial Policy Checklist.

Statistics

For all statistical analyses, confirm that the following items are present in the figure legend, table legend, main text, or Methods section.

n/a	Confirmed	
☐	☒	The exact sample size (*n*) for each experimental group/condition, given as a discrete number and unit of measurement
☐	☒	A statement on whether measurements were taken from distinct samples or whether the same sample was measured repeatedly
☐	☒	The statistical test(s) used AND whether they are one- or two-sided *Only common tests should be described solely by name; describe more complex techniques in the Methods section.*
☒	☐	A description of all covariates tested
☐	☒	A description of any assumptions or corrections, such as tests of normality and adjustment for multiple comparisons
☐	☒	A full description of the statistical parameters including central tendency (e.g. means) or other basic estimates (e.g. regression coefficient) AND variation (e.g. standard deviation) or associated estimates of uncertainty (e.g. confidence intervals)
☐	☒	For null hypothesis testing, the test statistic (e.g. *F*, *t*, *r*) with confidence intervals, effect sizes, degrees of freedom and *P* value noted *Give P values as exact values whenever suitable.*
☒	☐	For Bayesian analysis, information on the choice of priors and Markov chain Monte Carlo settings
☒	☐	For hierarchical and complex designs, identification of the appropriate level for tests and full reporting of outcomes
☐	☒	Estimates of effect sizes (e.g. Cohen's *d*, Pearson's *r*), indicating how they were calculated

Our web collection on statistics for biologists contains articles on many of the points above.

Software and code

Policy information about availability of computer code

Data collection	Flow cytometry data was collected with BD LSRFortessa and FACSymphony A5 with BD FACSDiva Software v9.3.1.
Data analysis	Data analysis was done with Flowjo v10.10.0, Loupe Broswer v8.0.0, Xenium Explorer v3.2, GraphPad Prism v10.4.1, iRmap (proprietary software of iRepertoire, version unknown), IgPhyml v4.0.0, and alakazam v1.3.0..

For manuscripts utilizing custom algorithms or software that are central to the research but not yet described in published literature, software must be made available to editors and reviewers. We strongly encourage code deposition in a community repository (e.g. GitHub). See the Nature Portfolio guidelines for submitting code & software for further information.

Data

Policy information about availability of data

All manuscripts must include a data availability statement. This statement should provide the following information, where applicable:

- Accession codes, unique identifiers, or web links for publicly available datasets
- A description of any restrictions on data availability
- For clinical datasets or third party data, please ensure that the statement adheres to our policy

The data supporting the findings of this study are available in the article. Spatial transcriptomic datasets have been deposited for mouse at https://doi.org/10.5281/zenodo.17346168 and human at https://doi.org/10.5281/zenodo.17354774. BCR sequencing datasets have been deposited at https://doi.org/10.5281/zenodo.17345590. A reference library was used for mapping BCR sequences to germline V, D, J, and C sequences (IMGT, https://www.imgt.org/) and cell annotation databases were utilized for manual annotation of graph-based clusters (ACT, http://biocc.hrbmu.edu.cn/ACT/; PanglaoDB, https://panglaodb.se/).

Research involving human participants, their data, or biological material

Policy information about studies with human participants or human data. See also policy information about sex, gender (identity/presentation), and sexual orientation and race, ethnicity and racism.

Reporting on sex and gender	Data reported in Table S1. Of n=19 individuals, our study included n=12 males, n=5 females, and n=2 for which gender was not collected.
Reporting on race, ethnicity, or other socially relevant groupings	Race and ethnicity were not collected for the human subjects in this study.
Population characteristics	Individuals included in this study were undergoing orthotopic liver transplantation at Emory Transplant Center of Emory University Hospital or at Massachusetts General Hospital. Patients were chronically infected with HCV or HBV without coinfection with HIV. Liver tissue was also obtained from individuals with HCC or with no apparent hepatic disease as indicated in Supplementary Table S2.
Recruitment	Patients involved in this study gave written informed consent in accordance with IRB #00100485 (Emory), IRB #1999P004983 (Mass General Brigham), and #2004P000793 (Mass General Brigham). Patients from Emory University or the Emory Clinic with liver diseases that may lead to liver failure or recipient candidates for liver transplantation were identified for potential inclusion in the study by attending transplant physicians. They were approached by a transplant research coordinator, attending transplant physician, or surgeon for participation in the study and gave informed consent. The procedures and assays involved in the study had no impact on clinical outcome or clinical management. Since participants were first approached by transplant physicians based on aforementioned selection criteria, there may be selection bias for patients with more severe liver disease. However, this is unlikely to impact our study given our study was focused on liver disease and thus required samples from patients with these respective conditions.
Ethics oversight	Written informed consent was obtained from each patient and IRB #00100485 conforms to the guidelines of the 1975 Declaration of Helsinki (revised 2013). Additional human liver samples were obtained in accordance with the protocol approved by the Mass General Brigham IRB, protocol #1999P004983 and #2004P000793.

Note that full information on the approval of the study protocol must also be provided in the manuscript.

Field-specific reporting

Please select the one below that is the best fit for your research. If you are not sure, read the appropriate sections before making your selection.

☒ Life sciences ☐ Behavioural & social sciences ☐ Ecological, evolutionary & environmental sciences

For a reference copy of the document with all sections, see nature.com/documents/nr-reporting-summary-flat.pdf

Life sciences study design

All studies must disclose on these points even when the disclosure is negative.

Sample size	Sample size calculation was not performed to predetermine sample size. Sample sizes were chosen rationally based on pilot experiments and numbers typical to the field for subsequent experiments. The n numbers for independent experiments used in the study are noted in the figure legends.
Data exclusions	No data were excluded.
Replication	Graphs include representative or pooled data from independent experiments specifically detailed in each figure legend.
Randomization	Age-matched mice of identical strains ordered from commercial vendors were randomly divided into cages by animal care staff upon arrival at vivarium facilities. Mice were further randomly divided into groups upon initiation of experiments. Group allocation for genetically modified mice (e.g. B1-8i) was based on genotype so groups were not randomized.
Blinding	Blinding was not performed in this study because most readouts (e.g. RT-qPCR, FACS) are not subjective and the same personnel who performed the experiments analyzed results.

Reporting for specific materials, systems and methods

We require information from authors about some types of materials, experimental systems and methods used in many studies. Here, indicate whether each material, system or method listed is relevant to your study. If you are not sure if a list item applies to your research, read the appropriate section before selecting a response.

Materials & experimental systems

n/a	Involved in the study	
☐	☒	Antibodies
☐	☒	Eukaryotic cell lines
☒	☐	Palaeontology and archaeology
☐	☒	Animals and other organisms
☒	☐	Clinical data
☒	☐	Dual use research of concern
☒	☐	Plants

Methods

n/a	Involved in the study	
☒	☐	ChIP-seq
☐	☒	Flow cytometry
☒	☐	MRI-based neuroimaging

Antibodies

Antibodies used

All antibodies listed below are anti-mouse unless specified.

Flow cytometry antibodies (Marker, Conjugation, Clone, Dilution, Source, Catalog number, Lot number): CD16/CD32 (Fc shield), Unconjugated, 2.4G2, 1:100, Tonbo, 70-0161-U100, P0161060524704; CD19, BV421, 6D5, 1:100, Biolegend, 115538, B424043; TCRbeta, BUV395, H57-597, 1:100, BD Horizon, 569248, 5091099; CD138, BV605, 281-2, 1:100, Biolegend, 142516, B448799; CD38, PE, 90/CD38, 1:100, BD Pharmingen, 553764, 4246159; CD95, PE-Cy7, Jo2, 1:100, BD Pharmingen, 557653, 4260072; CD4, BV650, GK1.5, 1:100, Biolegend, 100469, B388323; CD279 (PD-1), BV785, 29F.1A12, 1:100, Biolegend, 135225, B415811; CD185 (CXCR5), Biotin, SPRCL5, 1:50, eBioscience,13-7185-82, 2885829

ELISpot antibodies (Marker, Conjugation, Clone, Application, Dilution, Source, Catalog number, Lot number): IgG H+L, Unconjugated, Polyclonal, Coating, 10 µg/mL, Jackson, 115-005-166, 170576; Fcgamma, HRP, Polyclonal, Detection, 1:1000, Jackson, 115-035-008, 170836; anti-(Human) IgG, Unconjugated, MT91/145, Coating, 10 µg/mL, Mabtech, 3850-3-250, 12.4; anti-(Human) IgG, Biotin, MT78/145, Detection, 1:500, Mabtech, 3850-6-250, 9.1

In vivo antibodies (Marker, Clone, Source, Catalog number, Lot number): CD40L, MR1, InVivoMab, BE0017-1, 810121N1; VLA-4, PS/2, InVivoMab, BE0071, 844123D1; LFA-1, M17/4, InVivoMab, BE0006, 834022M2; Osteopontin (SPP1), MPIIIB10, InVivoMab,BE0382, 812623J3

Validation

Validation; All antibodies used in this study were obtained from reliable vendors and validation is provided on their respective websites as shown below:
CD16/CD32 (Fc shield): https://cytekbio.com/products/purified-anti-mouse-cd16-cd32-2-4g2-fc-block?variant=40581190713380
CD19: https://www.biolegend.com/en-gb/products/brilliant-violet-421-anti-mouse-cd19-antibody-7160?GroupID=BLG10556
TCRbeta: https://www.bdbiosciences.com/en-us/products/reagents/flow-cytometry-reagents/research-reagents/single-color-antibodies-ruo/buv395-hamster-anti-mouse-tcr-chain.569248?tab=product_details
CD138: https://www.biolegend.com/fr-lu/products/brilliant-violet-605-anti-mouse-cd138-syndecan-1-antibody-8730
CD38: https://www.bdbiosciences.com/en-us/products/reagents/flow-cytometry-reagents/research-reagents/single-color-antibodies-ruo/pe-rat-anti-mouse-cd38.553764?tab=product_details
CD95: https://www.bdbiosciences.com/en-us/products/reagents/flow-cytometry-reagents/research-reagents/single-color-antibodies-ruo/pe-cy-7-hamster-anti-mouse-cd95.557653?tab=product_details
CD4: https://www.biolegend.com/en-gb/products/brilliant-violet-650-anti-mouse-cd4-antibody-16780?GroupID=BLG4211
CD279 (PD-1): https://www.biolegend.com/de-at/products/brilliant-violet-785-anti-mouse-cd279-pd-1-antibody-9874?GroupID=BLG7927
CD185 (CXCR5): https://www.thermofisher.com/antibody/product/CD185-CXCR5-Antibody-clone-SPRCL5-Monoclonal/13-7185-82
IgG H+L: https://www.jacksonimmuno.com/catalog/products/115-005-166
Fcgamma: https://www.jacksonimmuno.com/catalog/products/115-035-008
anti-IgG (Human, MT91/145): https://www.mabtech.com/products/anti-human-igg-mabs-mt91145-unconjugated-3850-3
anti-IgG (Human, MT78/145): https://www.mabtech.com/products/anti-human-igg-mabs-mt78145-biotin-3850-6
CD40L: https://bioxcell.com/invivomab-anti-mouse-cd40l-cd154-be0017-1
VLA-4: https://bioxcell.com/invivomab-anti-mouse-human-vla-4-cd49d-be0071
LFA-1: https://bioxcell.com/invivomab-anti-mouse-lfa-1-alpha-cd11a-be0006
Osteopontin (SPP1): https://bioxcell.com/invivomab-anti-mouse-human-rat-osteopontin-spp1

Eukaryotic cell lines

Policy information about cell lines and Sex and Gender in Research

Cell line source(s)

HEK293T cells were purchased from ATCC (CRL-3216).

Authentication

This cell line was only used to produce RHV E2 monomer for this study, which was confirmed successful. No further authentication other than noting of consistent morphology was done aside from what was performed by the vendor.

Mycoplasma contamination

Cells were authenticated and tested negative for mycoplasma contamination by vendor.

Commonly misidentified lines (See ICLAC register)

No commonly misidentified cell lines were used in this study.

Animals and other research organisms

Policy information about studies involving animals; ARRIVE guidelines recommended for reporting animal research, and Sex and Gender in Research

Laboratory animals

C57BL/6J, B6.129P2-Aicdatm1(cre)Mnz/J, and B6.129P2[C]-Ighm2Cgn/J mice at 6-10 weeks of age were utilized in this study in accordance with approved protocols from the Emory Institutional Animal Care and Use Committee (IACUC #201700372). Animals were housed with access to food and water ad libitum at a temperature of 68-75 F and humidity of 35-65% with a 12-hour light/dark cycle.

Wild animals

No wild animals were used in this study.

Reporting on sex

All mice utilized in this study were female.

Field-collected samples

No field-collected samples were used in this study.

Ethics oversight

All biohazard and animal experiments were carried out in accordance with approved protocols from the Emory Institutional Animal Care and Use Committee (IACUC #201700372).

Note that full information on the approval of the study protocol must also be provided in the manuscript.

Plants

Seed stocks

n/a

Novel plant genotypes

n/a

Authentication

n/a

Flow Cytometry

Plots

Confirm that:

☒ The axis labels state the marker and fluorochrome used (e.g. CD4-FITC).

☒ The axis scales are clearly visible. Include numbers along axes only for bottom left plot of group (a 'group' is an analysis of identical markers).

☒ All plots are contour plots with outliers or pseudocolor plots.

☒ A numerical value for number of cells or percentage (with statistics) is provided.

Methodology

Sample preparation	Cells from all organs were passed through 70 micron strainers, with all organs being mashed with a plunger, with the exception of bone marrow being flushed through the bone with RPMI. All organs, with the exception of lymph nodes, were then lysed with ACK RBC lysis buffer. Intrahepatic leukocytes were isolated via Percoll centrifugation, as described in detail in the Methods section. All cell pellets were washed and resuspended in fresh media for counting.
Instrument	Samples were acquired on BD LSRFortessa and FACSymphony A5.
Software	Software used for sample acquisition was BD FACSDiva Software.
Cell population abundance	Mean frequencies of GC B cells, Tfh, and plasma cells from RHV-infected livers at week 4 post-infection were 19.21%, 5.89%, and 4.26%, respectively.
Gating strategy	Detailed gating strategies are described in detail in Fig. S1, S2, and S3. Briefly, GC B cells were defined as CD38lowCD95high B cells, plasma cells were defined as CD38lowCD138+ CD19+ cells, and Tfh were defined as CXCR5+PD-1+ CD4 T cells.

☒ Tick this box to confirm that a figure exemplifying the gating strategy is provided in the Supplementary Information.